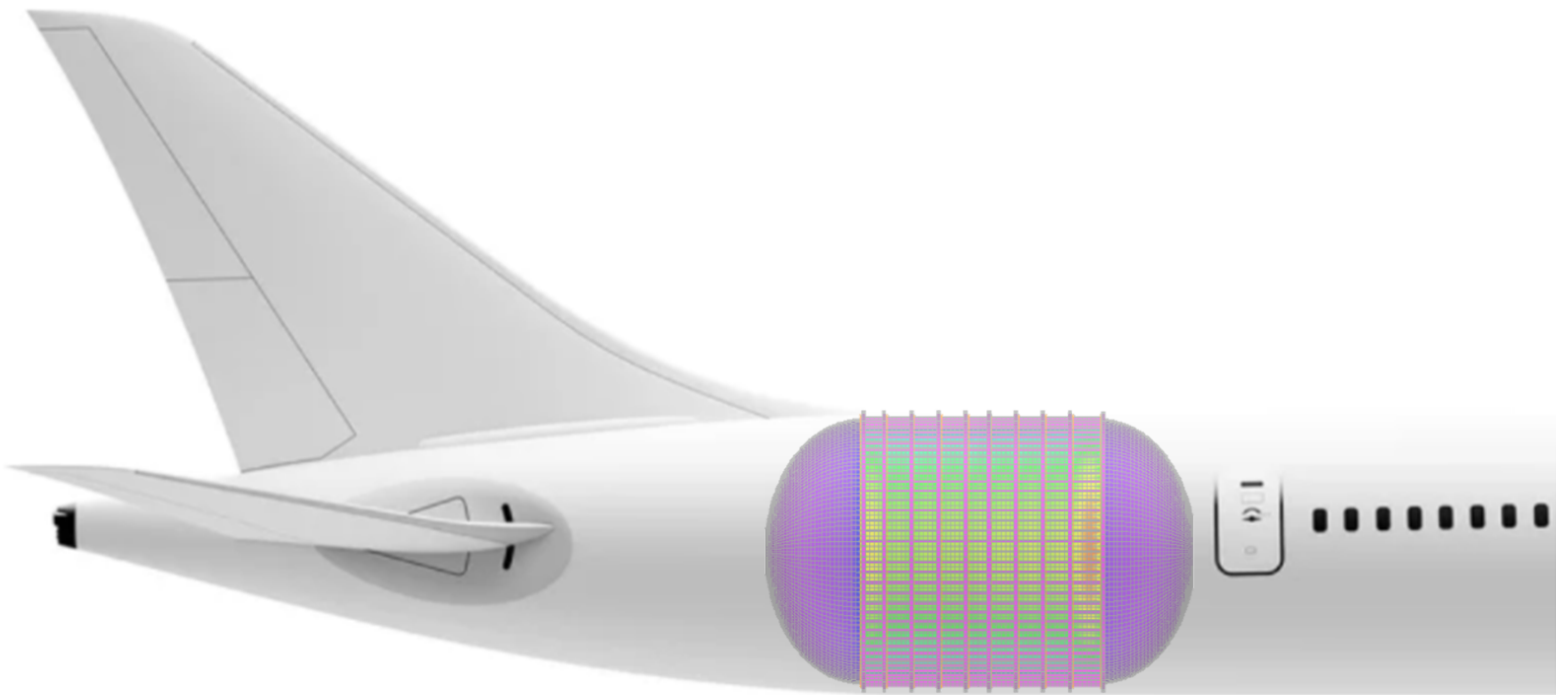# Structural Analysis of a New Integral Tank Concept for Hydrogen Storage On-board Commercial Aircraft

MSc Thesis Aerospace Engineering

Tomás Montellano

TUDelft

Delft
University of
Technology

Challenge the future

Structural Analysis of a New Integral Tank Concept for Hydrogen Storage On-board Commercial Aircraft

MSc Thesis Aerospace Engineering

by

Tomás Montellano

For obtaining the degree of Master of Science in Aerospace Engineering at Delft University of
Technology,
to be defended publicly on Friday April 26, 2024 at 09:00 AM.

Student number: 4890132
Thesis committee: Dr. ir. M.F.M. (Maurice) Hoogreef,   TU Delft, Supervisor
                    Dr. ing. A. (Alexander) Heidebrecht,   TU Delft, Supervisor
                    Dr. ir. J.M.J.F. (Julien) van Campen,   TU Delft, Examiner
                    Dr. C. (Carmine) Varriale,   TU Delft, Chair

TUDelft
Delft
University of
Technology

PREFACE

This master's thesis marks the end of a journey that began in 2014, in Portugal. As I started my studies in aerospace engineering, I could not have foreseen the twists and turns that would lead me to this moment. However, reflecting on the last 10 years, I can confidently say that all the experiences along the way were worth it and I have no regrets about embracing the challenges that came my way.

First and foremost, I would like to tank my supervisors, Maurice and Alexander, for the guidance throughout this project. They gave me the autonomy to lead the project, while providing valuable advice in the right moments. I enjoyed all of our discussions, which were instrumental in shaping this thesis. I extend my gratitude to Saullo Castro for generously sharing his expertise in structural analysis.

I am also grateful to my family and friends back home. Although a significant part of this time was at a distance, I have always felt their unwavering support. To my friends in the Netherlands, the experiences shared with you greatly enriched my academic and personal life and I surely hope to keep in touch with all of you. A special thanks goes to my housemates in Rotterdam and to the daily companions of room NB.109.

Lastly, I would like to thank my girlfriend for always believing in me. It is with excitement that I start a new journey back in Portugal and I am looking forward to sharing the new challenges with you.

Tomás Montellano
Delft, April 2024

SUMMARY

Growing concerns about the environmental impact of aviation have sparked interest in hydrogen aircraft as a greener alternative. Hydrogen can be used to power existing turbofan engines or electrical motors via a fuel cell, eliminating carbon emissions not only during flight, but also during production, provided renewable energy sources are used. However, adopting hydrogen as fuel introduces technological challenges, particularly with regard to on-board storage. Integral tanks, which are part of the aircraft's main structure, seem promising but existing designs show limitations in their integration with the airframe and insulation capabilities.

To address these issues, this study proposes an integral tank concept featuring a double wall architecture with vacuum insulation. The main advantage of this design is the use of an external stiffened wall that can be directly connected to the remaining airframe. In addition, having stiffeners on the outside ensures the required space for systems routing and addresses concerns with the crash worthiness of the structure. A parametric method, coupled with finite element analysis is developed to size the external load bearing wall, enabling quick analysis and mass estimations of different tank configurations. The method consists of a sizing optimization with the objective of minimizing the structural mass under constraints on the strength, buckling stability and fatigue behaviour.

The feasibility of the concept is then evaluated on an aft tank for a short/medium range aircraft in configurations with and without a forward tank. Preliminary results under this realistic scenario point to fuel containment efficiencies of up to 0.71, which are consistent with existing designs. Moreover, buckling stability is identified as the critical design criterion, highlighting the importance of using a stiffened shell design. These findings show the viability of the proposed concept from a structural standpoint and provide the basis for further research. The optimum solution at an aircraft level can be obtained by integrating the developed framework into a multidisciplinary aircraft design tool.

CONTENTS

LIST OF FIGURES

LIST OF TABLES

NOMENCLATURE

Abbreviations

AFT   After/Behind

CG   Center of Gravity

CS   Certification Specifications

DOE   Design of Experiments

DSG   Design Service Goal

EASA European Aviation Safety Agency

FAR   Federal Aviation Regulation

FC   Fuel Containment

FE   Finite Element

FM   Fuel Mass

FWD Forward

IWTI Inner Wetter Thermal Insulation

KBE   Knowledge Based Engineering

MLI   Multi-Layer Insulation

MOP   Maximum Operating Pressure

MTOM   Maximum Take Off Mass

MZFM   Maximum Zero Fuel Mass

NASA   National Aeronautics and Space Administration

NLR   Netherlands Aerospace Centre

OEM   Operational Empty Mass

OOP   Object Oriented Programming

PM   Payload Mass

SEC   Specific Energy Consumption

SF   Safety Factor

SLS   Space Launch System

$SOFI$ Spray-On Foam Insulation

$USSR$ Union of Soviet Socialist Republics

$VD-MLI$ Variable Distance Multi-Layer Insulation

Symbols

β Slip angle

ΔP Pressure differential

η Efficiency

ν Poisson ratio

ρ Density

σ stress

τ Shear

A Area

b width

E Young's modulus

F, V, N Force

L Lift

l Length

M Moment

m mass

n_z Load factor

P Pressure

q Dynamic pressure

r Radius

T Thrust

t thickness

W Weight

Subscripts

ac Aerodynamic center

div Tank divider

emp Empennage

f Fairing

$fcargo$ Front cargo

fr Frame

fs Front spar

fus Fuselage

ht Horizontal tail

ins Insulation

MG Main landing gear

NG Nose landing gear

$rcargo$ Rear cargo

rs Rear spar

sk Skin

str Stringer

vt Vertical tail

w Wing

$wall_i$ Inner wall

$wall_o$ Outer wall

1

INTRODUCTION

With a specific energy almost three times higher than conventional kerosene, hydrogen has long been considered a promising aviation fuel that could allow aircrafts to fly farther and higher [1]. Particularly during the oil crisis of the 1970s, both the United States and the Soviet Union (USSR) launched programmes to test hydrogen propulsion on modified aircrafts [2–4]. Although successful flights showed the feasibility of hydrogen powered aircraft, investigations were abandoned due to the difficulty in handling hydrogen and the impact on airport logistics [5].

In recent years, increasing awareness about the environmental impact of aviation has renewed the interest in hydrogen aircraft. Hydrogen can be used to power existing turbofan engines or electrical motors via a fuel cell, eliminating carbon emissions not only during flight, but also during production, provided renewable energy sources are used [5]. In a time when conventional aviation is responsible for 3.5% of the net anthropogenic forcing [6], new sustainable projects as are gaining traction, choosing hydrogen as a solution to meet and possibly go beyond the industry's goal of net-zero carbon emissions by 2050 [7]. Perhaps the most prominent is Airbus ZEROe, which aims to bring commercial hydrogen aircraft to the market by 2035 [8].

However, using hydrogen as fuel presents novel technical challenges. Even in liquid form, hydrogen occupies four times the volume of kerosene, making on-board hydrogen storage the key factor for aircraft usability. While various options have been proposed, such as carrying hydrogen in dedicated fuel pods under the wings, the prevailing consensus is that tank(s) inscribed within the fuselage are the most efficient, reducing the aerodynamic and gravimetric penalties associated with tank integration [9]. In addition, these configuration enable the use of integral tanks, which are argued to have superior performance [10, 11]. In contrast to non-integral tanks which are independent "containers", the structure of integral tanks is integrated with the airframe and carries structural loads. The drawback with an integral tank approach is the added design complexity, as a stiffened structure is required to carry the loads of the primary fuselage structure. Hence, even though the majority of authors acknowledge the theoretical superiority of integral designs, the predominant approach in literature is to consider non-integral tanks [9, 12, 13]. This allows researchers to explore a wide variety of designs and the influence of different parameters, regardless of the precise aircraft for which the tanks are designed. Studies on integral tanks exist but current solutions rely on single wall architectures that compromise the integration with the airframe or the insulation capabilities of the tank, hindering their adoption in practical applications. [3, 14].

1.1. PROJECT GOAL AND RESEARCH QUESTIONS

In this research, a new solution is proposed that applies a double wall construction to integral tank design. In this concept, vacuum is maintained between the walls, with the external wall being directly bolted to the to the primary airframe. The primary goal of this study is to evaluate the feasibility of the new proposed concept by comparing its performance against other designs. Given the importance of weight in aircraft design, a mass based evaluation parameter seems an appropriate choice for this thesis. The widely accepted metric to measure tank performance is the gravimetric efficiency of the tank, as defined in equation 1.1.

$$\eta_{grav} = \frac{m_{LH2}}{m_{LH2} + m_{tank}} \tag{1.1}$$

Where m_{H_2} is the hydrogen fuel mass and m_{tank} is the mass of the empty tank. However, a review of current literature showed that a large spectrum of gravimetric efficiencies ranging from 0.25 to 0.85 can be found [15], which is attributed to the lack of consistency in defining the terms in equation 1.1. To provide clarity in the mass estimation, the definition in equation 1.2 is used in this research, where m_{LH_2} includes unused fuel and possible vented fuel and m_{FC} concerns only the mass related to the fuel containment (FC). A more detailed description of each term is provided in chapter 3.

$$\eta_{FC} = \frac{m_{LH2}}{m_{LH2} + m_{FC}} \tag{1.2}$$

With this in mind, the main research question of this thesis is:

How does the fuel containment efficiency of an integral tank compare to existing concepts, when using vacuum insulation and a stiffened external shell?

Answering the research question entails the development of a method capable of providing accurate mass estimations of the integral tank concept, with particular attention to the tank structure that must be sized to handle the loads of the primary structure. It is therefore appropriate to establish the followings sub-questions:

1. How can the load bearing structure of the integral tank be sized?

2. What variables and design criteria have the biggest impact on the tank mass?

Besides showing the feasibility of the proposed solution, this work also aims to establish trends and guidelines that can be applied to the first generation of hydrogen aircraft, motivating further research and contributing to an earlier adoption of this technology.

1.2. PROJECT APPROACH

In the few cases where integral tanks have been considered for their advantages, the focus was on determining the impact of tank integration at an aircraft level, with tank sizing methods mostly limited to pressure vessel calculations [9, 16]. Also, few details are given on how the tank is connected to the aircraft structure. The studies by Brewer and Gomez are notable exceptions where the sizing of the stiffening structure was explicitly addressed [3, 14]. However, the solutions presented in these studies are confined to the specific aircraft under investigation. It is then desirable to have a method based on a parametric framework, which is capable of quickly generating and providing mass estimations of different tanks.

The method proposed in this research is developed on a standalone basis, with the potential to be incorporated into a multidisciplinary aircraft tool at a later stage to achieve an optimum solution

for an hydrogen aircraft. To validate the method effectively, it's crucial to select a realistic scenario in terms of tank geometry and sizing loads. The aircraft-level studies mentioned provide an ideal platform, as they already incorporate necessary aircraft changes to accommodate hydrogen tanks, including updates to wing, empennage, engine, and landing gear geometry [9]. Among the different studies prospected, the hydrogen aircraft generated by Onorato stand out, not only in terms of data available but also in the level of detail in the analysis. Onorato modified TU Delft aircraft synthesis programme to allow for the design and analysis of hydrogen fueled aircraft [16]. In particular, the aircraft generated in the short/medium range, based on the A320 was chosen. Based on these aircraft, the loads acting on the airframe can be determined and used to size the tank structure and estimate its mass.

In aircraft design, different mass estimation methods can be used depending on the data required and level of accuracy desired [17]. At early development stages, lower-order methods (I and II) are commonly favored but such methods are based on empirical and statistical data, which is not available in literature for integral tanks. In this thesis, a more accurate method following a finite element (FE) approach is used, corresponding to a class III method. While this choice reduces the flexibility to study design changes, it is appropriate for this research due to the level of detail already included in the proposed structural solution. In order to reduce the inherent computational cost of the FE analysis, simplifying assumptions are used to represent the tank structure in such a way that can be studied.

1.3. PROJECT SCOPE

LIQUID HYDROGEN

In this thesis, only liquid hydrogen is considered. While compressed hydrogen has gained momentum in the automotive industry, its energy density is nearly two times lower in comparison with liquid hydrogen, even at 700 bar. Higher pressures are possible but the increased demand on the tank structure results in a heavier pressure vessel that voids any gain in energy density [18].

For this reason, gaseous hydrogen is only considered in aviation for small regional aircrafts. For instance, ZeroAvia, one of the leading companies in hydrogen aviation, uses two compressed hydrogen tanks to fuel its Dornier 228 testbed aircraft with a range of 300 NM [19]. However, for larger aircrafts with ranges of 1000 NM and more, ZeroAvia and other industry players including Airbus agree that cryogenic liquid hydrogen, which can be stored at near ambient pressures, is the best solution [8].

CONVENTIONAL AIRCRAFT

This research is also limited to conventional tube-and-wing aircraft. While future aircraft concepts such as TU Delft's Flying-V or Airbus's blended wing body (BWB) can be conveniently designed with hydrogen in mind and provide extra volume for storage [8, 20], there is a considerable certification burden associated with changing both the propulsion system and the aircraft configuration. It is therefore a reasonable assumption that early hydrogen aircraft will use conventional tube-and-wing configurations.

1.4. REPORT STRUCTURE

This report is organized into 6 chapters with the following structure: Chapter 2 starts by describing the key challenges and reviewing the current state of the art in integral tank designs. It is here that the new concept is proposed. Chapter 3 explains the methodology used in this study, detailing how the sizing loads are estimated and how the tanks are sized. Chapter 4 focuses on validating the proposed framework. This sets the stage for chapter 5, which presents and discusses the results, sharing insights from load design trends and sensitivity analyses. Finally, Chapter 6 wraps up with a synthesis of the main conclusions, along with recommendations for future research.

2

ON-BORD CRYOGENIC STORAGE

The main disadvantage with using liquid hydrogen is that it boils at a temperature around 20k. As hydrogen boils, the pressure inside the tank rises until it eventually becomes necessary to release hydrogen to prevent a structural failure of the tank. This process is known as venting and the released hydrogen is usually lost unless a complex recovery system is in place [3]. In order to avoid excessive boil-off, an effective insulation is required to reduce heat transfer into the tank and maintain cryogenic conditions.

Even though liquid hydrogen is new in aviation, is has already been extensively used in space applications such as space launchers. Nevertheless, the differences in sector requirements do not allow a direct transfer in technology. During launches, hydrogen is consumed very quickly, which lessens the insulation requirements and allows boil-off rates of approximately 1.6% by weight per hour [21]. Moreover, most designs such as the space shuttle external tank are expendable and developed for single use. On the contrary, an acceptable boil-off rate in aviation is in the order of 0.1% by weight per hour [21], and the tank must be designed for the full service life of the aircraft [10]. Therefore, although space applications advanced the knowledge and technology for cryogenic hydrogen storage, a new approach is required for aircraft applications.

This chapter will provide an overview of the key design choices available to the researcher, which influence the tank performance. These choices include the tank shape, aircraft layout, insulation methods and materials. In addition, the existing integral tank concepts are reviewed. Based on the challenges and issues identified, the chapter closes with a proposal of a new integral tank concept, which will be the main focus of this research.

2.1. TANK SHAPE AND AIRCRAFT CONFIGURATION

The shape of the tank is relevant for thermal and structural reasons. On one hand, selecting a shape that minimizes the tank's surface area for a given volume decreases heat transfer with the exterior, and consequently, insulation requirements [21]. From that perspective, a sphere is the preferable shape since it has the lowest surface to volume ratio. However, that advantage decreases as the tank volume increases, as shown by Adler in figure 2.1 [18].

On the other hand, tanks with circular cross sections are more efficient in handling the pressure loads associated with fuel containment and can reduce the bending stresses within the tank wall. As a result, thinner walls can be used, and lower tank weights can be achieved. In a parametric study,
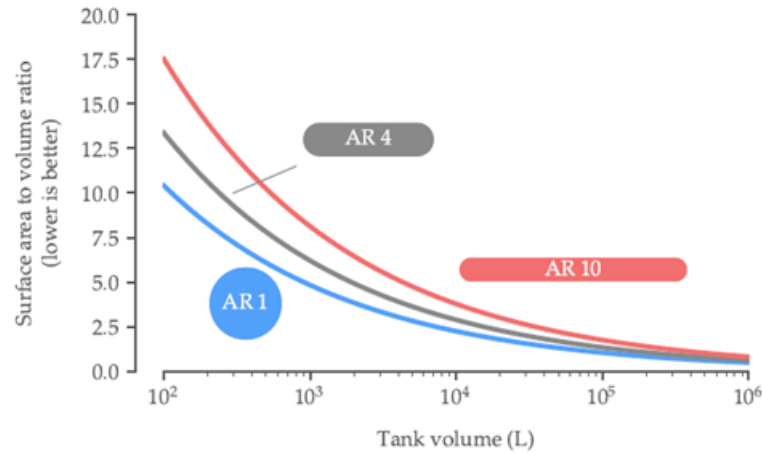
Figure 2.1: Impact of tank volume on surface area to volume ratio (AR). Extracted from [18].

Winnefeld showed that as one deviates from the optimum spherical shape, the tank wall thickness can increase up to five times [12]. Moreover, the differences in FC efficiency would be even higher due to the increased surface area to volume ratio of non-spherical shapes.

Although the paragraphs above make a compelling case for a spherical shape, hydrogen tanks are nearly always cylindrical, maintaining the optimum circular cross section but facilitating manufacturing and integration. The cylinder is then enclosed by end caps that are usually hemispherical, ellipsoidal or torispherical.

Finally, accommodating the large volumes required by hydrogen in a confined aircraft space is a major technological challenge. Current aircraft structures are designed to carry jet fuel and retrofitting hydrogen tanks usually results in payload, drag and weight penalties [18]. In conventional aircraft, storing hydrogen inside the wings as is done with jet fuel would result in tanks with a large surface to volume ratio, which explains why this solution is not found in literature. The exception is a study in 1955 by Silverstein and Hall but here, the focus was on evaluating the feasibility of using liquid hydrogen as fuel for jet-engines and not on developing efficient storage solutions [1].

Generally, hydrogen tanks can be carried in dedicated fuel pods or integrated in the aircraft's fuselage. Podded tanks offer operational, safety and maintenance advantages since the aircraft length is maintained and the tanks are located outside of the passenger cabin, making them more accessible for inspection/repairs [16]. Moreover, if placed under the wings, tanks are close to the aircraft's centre of gravity, offering a bending moment alleviation effect on a now dry wing-box and reducing the structural mass of the wing [22]. Nevertheless, the clear disadvantages of this option are the reduced ground clearance and the strong increase in aerodynamic drag. Studies by Silberhorn and Troeltsch predicted a 10% higher fuel consumption in comparison with a configuration with tanks inscribed in the fuselage [9, 23].

Regarding fuselage mounted tanks, three configurations are commonly found in literature, as shown in figure 2.2. Accommodating the large tanks requires a reduction in passenger capacity or a change in the fuselage shape, with the latter leading to an increase in fuselage drag and structural mass. In addition, a fuselage extension affects airport operations and usually entails an increase in the landing gear mass to ensure the same rear clearance [9].

Figure 2.2: Common hydrogen storage solutions in tube-and-wing aircraft. Extracted from [18]

In the simplest configuration, a single tank is positioned behind the cabin and the rear pressure bulkhead (hereinafter referred to as AFT tank). The main limitation of this option is the variation in center of gravity (CG) position as hydrogen is consumed, which introduces trim and stability issues. This reason leads multiple studies to agree that the layout with a single AFT tank is only suitable for short range and regional aircraft in which the fuel is a small fraction of the overall aircraft weight [24].

In larger aircraft, an additional tank must be placed in front of the passenger cabin to limit the shift in CG (hereinafter referred to as FWD tank). Since the FWD tank separates the cockpit from the cabin, a small passage is required to ensure pilots always have access to the cabin and the passengers can evacuate the aircraft in the time required by aviation standards. [25]. As shown by Gomez, providing this passage with an integral tank design would require additional reinforcements leading to significant increase in structural mass [14]. For this reason, FWD tanks are usually non-integral.

Another possible configuration positions the tanks above the fuselage. This concept shares some of the advantages of podded tanks including maintaining the original aircraft length and having the tanks near the CG of the aircraft but, crucially, also incurs a heavy drag penalty. In the Cryoplane study, aircraft using this concept were estimated to have a 10% higher Specific Energy Consumption (SEC) and a 30% higher Operational Empty Weight (OEW) compared to the kerosene equivalent [24].

Based on the information provided summarizing the current literature knowledge, the following sections will focus on tanks inside the fuselage cross section, which are seen as the most promising candidates for early hydrogen aircraft.

2.1.1. Insulation and Wall Architecture

As mentioned above, one of the critical aspects in cryogenic tank design is maintaining hydrogen in a temperature below its boiling point, even with the temperature difference between the exterior and interior of the tank reaching values of 300°C. Although active refrigeration systems could be used, their added weight and complexity makes them more suitable for large stationary applications. For mobile applications where weight is crucial, a passive insulation system should be applied [10].

According to Mital, who conducted an extensive review on tank materials, effective insulation systems for aviation must have a low thermal conductivity, low diffusivity and low density [21]. Based on these criteria, both polymer foams and multi-layer insulations (MLI) stand out. Foam insulation has been widely used in space applications. It has the advantage of being easier to model due to its well-known properties and is typically used as Spray-on foam insulation (SOFI), which is applied on the outside of the tank wall. In aircraft applications, a combination of closed and open-cell foam has been suggested by Brewer [10] and adopted in multiple investigations [9, 11, 12, 16].

On the other hand, MLI consists of alternating layers of reflective shields and low conductivity spacers to minimize the radiative heat transfer through the tank. The radiation shields are often constructed of aluminized or goldized Mylar, while the spacers are typically made of polyester, glass

fiber paper, or silk [26]. Also referred to as "vacuum insulation", MLI is drastically more efficient when operating at vacuum conditions, achieving thermal conductivity values about 100 times lower than foam insulations [11]. The higher thermal performance of MLI enables a better control of the tank pressure, allowing the aircraft to stay on ground for extended periods of time. While it is not clear what is the required dormancy time, with values between 2h and 36h found in literature, Huete concludes that venting at the airport should be avoided during early stages of hydrogen aviation due to safety and operational concerns [27].

The disadvantage usually pointed to vacuum MLI designs is the requirement to have a double wall construction to hold the vacuum, with researchers claiming a lighter design could be achieved with a single wall design using foam insulation. However, there is an argument to be made that a double wall construction is always required, even with foam insulation. In typical single wall designs, SOFI is applied on the exterior of the stiffened tank wall. Due to the cryogenic temperatures, air trapped inside the foam may solidify, creating a vacuum that pulls in more air in a phenomenon known as cryopumping [28]. Also, the cold foam becomes brittle and is prone to develop cracks as the aircraft vibrates under normal operation. These effects contributed to the failure of NASA's X-33 prototype and must be avoided by using vacuum or purging the air with an inert gas such as helium, hence requiring a double wall construction. Following this reasoning, Mital concluded that "a double wall construction with a vacuum-based insulation system may turn out to be an optimum system (…)" [21].

A problem for vacuum insulations is the drastic decrease in thermal insulation if vacuum is lost. In this case, the heat entering the tank would require hydrogen to be released in a matter of minutes, which constitutes a serious safety hazard [29]. Nevertheless, such risk can be mitigated by having redundant vacuum pumps, which is a standard practice in the aerospace industry [27]. Also, recent research is improving the insulation performance of MLI, even without vacuum, by varying the distance between spacers (VD-MLI) or by integrating foam layers in the insulation [30]. A schematic representation of MLI and VD-MLI is presented in figure 2.3.
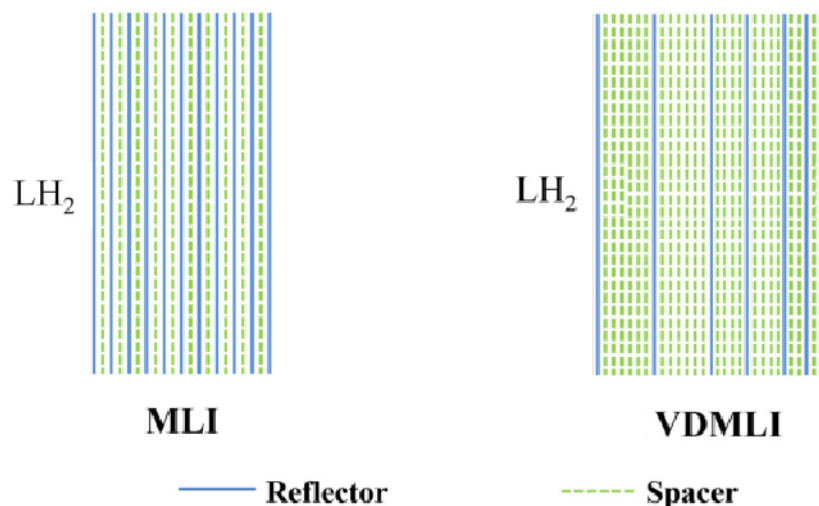

Figure 2.3: Structure of MLI and VD-MLI, adapted from [30]

It is worth noting that some investigations consider foam insulation applied on the interior of the tank. One interesting case is the design of an integral tank by Gomez and Smith [14], in which Inner Wetted Thermal Insulation (IWTI) is applied. Although liners are used to avoid direct contact of the

insulation with the cryogenic hydrogen, it is challenging to completely prevent hydrogen permeation through the insulation layers, which would ruin the insulation [10]. Also, foam embrittlement due to the cryogenic temperatures would be more severe in this configuration. Again, internal insulation has only been successfully used in space applications such as the third stage of the Saturn V's rocket [21].

2.1.2. Pressure Management

While heat entering the tank will increase the tank pressure, hydrogen withdrawal by the engines has the opposite effect. Therefore, a careful balance between the desired dormancy time and the fuel flow for a certain mission is required. According to Huete et al, designing for no pressure variation during cruise would result in a dormancy time of approximately 60% of the cruising time, but if higher dormancy times are required, pressure is likely to decrease during cruise [27].

Models exist to predict the pressure fluctuations inside the tank, such as the simple homogeneous model from Lin et al, or the more accurate model proposed by Ramos [31]. However, for this research, it is more relevant to consider the extremes, both for safety and structural reasons. First, tank pressure should always be higher than atmospheric to prevent oxygen ingestion, which can lead to an explosive mixture. Thus, a minimum pressure of around 1.2 bar was suggested by Verstraete and adopted in various studies [11, 12, 16]. This pressure is usually also the filling pressure as it is desired to fill the tanks as the lowest allowable pressure and pressure is expected to rise before departure. On the other hand, the upper limit or the maximum allowable pressure (MOP) is the value used to size the internal vessel. Higher pressures demand stronger and heavier structures, decreasing the FC efficiency of the tank. Hence, the structural mass of vacuum insulated tanks is the lowest at the minimum allowed MOP [27].

2.1.3. Wall Materials

In the vast majority of cases and the ones relevant to this research, the internal tank structure is in direct contact with liquid hydrogen, which demands crucial characteristics from prospective wall materials. First, ideal materials must have suitable properties both at ambient and cryogenic temperatures [11]. Second and critically, they must have a low permeation to liquid and gaseous hydrogen [21]. Metals are the natural choice with a low permeation rate and an increase in physical properties such as yield strength at cryogenic temperatures [10]. While stationary applications mostly use steel due to its low cost and availability, aluminium alloys such as AL2219 are commonly selected for aircraft applications [12, 14, 20].

Given the demand for extremely light tanks, composite materials are promising candidates for tank walls and recent prototypes showed that mass savings of at least 75% relative to current aluminium tanks are possible [32]. This reduction is particularly relevant for long-range aircraft, which are the most affected by tank mass. The success of new designs comes from developing tanks that can have a low hydrogen permeation rate, without the need for a plastic or metallic liner. Liners used in previous designs not only increased the complexity and weight of the tanks but led to failure due to the mismatch in thermal expansion between the different materials, as reported in the X-33 project [21]. A study of particular interest is the research carried by Toray Advance composites (TAC) and Netherlands Aerospace Centre (NLR) in cooperation with partners from the industry and academia, which is developing a tank configuration with an MLI vacuum solution [33]. In a double wall configuration, composite materials can be used for just the inner vessel, outer vessel or both. Nevertheless, given the preliminary nature of this research, the materials of the inner and outer shells were limited to aluminium alloys used in aviation.

2.2. INTEGRAL TANK CONCEPTS

With an integral tank design, the tank itself is part of the airframe main structure, achieving a greater structural efficiency and a direct weight reduction, when compared to non-integral tanks. It also has a higher volumetric efficiency, contributing to a lower surface to volume ratio and minimizing either the fuselage radius or length, reducing overall drag. Finally, as the structure of the tank is more accessible, repairs and periodic maintenance can easily be carried.

However, integrating the tank structure with the remaining airframe, while providing good insulation capabilities is a complex challenge. This section discusses three integral tank concepts found in literature, reflecting different strategies to deal with these structural and thermal demands. Subsection 2.2.1 will detail the design of NASA's Space Lauch System (SLS) while subsections 2.2.2 and 2.2.3 will describe the concepts from Brewer and Gomez, respectively.

2.2.1. SPACE LAUNCH SYSTEM (SLS)

The SLS is NASA's most powerful rocket developed for deep space exploration and is currently in use for the Artemis lunar missions [34]. As depicted in figure 2.4, the two cryogenic tanks (liquid hydrogen and liquid oxygen) in SLS's core stage form part of the rocket primary structure, following the same configuration as the space shuttle's external tank and leveraging from the knowledge acquired during that programme.
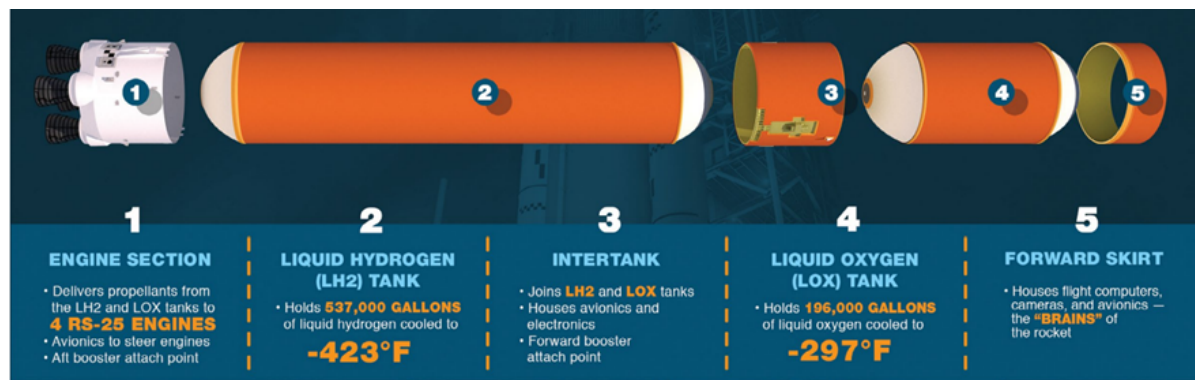
Figure 2.4: Exploded view of the main components in the core stage of SLS. Extracted from [34]

The integral structure allows the tanks to have a single wall design, maximizing its fuel capacity while reducing the overall mass of the rocket. In particular, the hydrogen tank is made of aluminium 2219 alloy and assembled in barrel sections, which are joined together by a process known as friction stir welding [34]. The tank is then connected to the remaining rocket sections using a bolted flange joint. Thermal protection is ensured by using SOFI on the exterior of the tank, which is machined to a thickness of approximately 3cm in the section of the hydrogen tank.

The FC efficiency of this particular hydrogen tank is not available in current literature but is assumed to be equal or higher to the hydrogen tank in the space shuttle's external tank, which was approximately 89% [18]. This assumption is supported by the improved manufacturing techniques used in the SLS such as using friction stir welding instead of fusion welding.

Although this design represents the current state of the art in lightweight cryogenic storage, it is only appropriate for space applications (for which it was designed). The short time that hydrogen is stored and the fact that the core stage is expendable (single use) allow for much higher boil-off rates and damages to the unprotected insulation, which do not meet the standards required for aviation.

Nevertheless, NASA conducted and funded several investigations concerning hydrogen storage for aircraft applications, with the most prominent tank design presented in the following subsection.

2.2.2. BREWER CONCEPT

Under NASA's sponsorship, various studies were conducted at Lockheed in the 1970's to evaluate the feasibility of hydrogen aircraft [2, 3]. These studies, headed by Richard Brewer, analysed both integral and non-integral tank designs for a subsonic aircraft with 400 passengers and a range of 5500NM. Based on the configuration seen in figure 2.5, Brewer concluded that integral tanks could provide structural mass savings of approximately two tonnes and have the advantage of easier access for maintenance purposes.

Similarly to the hydrogen tank in the SLS's core stage, the integral tank proposed by Brewer used a single stiffened wall made of 2219 aluminium alloy capped by two ellipsoidal ends. Being part of the fuselage primary structure, it was designed according to the requirements of the Federal Aviation Regulation, FAR 25, which sets the structural design criteria and loads that the airframe must handle. The critical difference to the previous concept was in the connection to the airframe structure. To avoid heat conduction through the structure that would lead to an excessive boil-off rate, the tank was connected to the fuselage airframe by a truss-like structure consisting of a series of boron-reinforced fiberglass tubes. According to Brewer, this intricate design maximized stiffness while minimizing heat transfer [10]. A schematic of the tank's structural concept can be seen on figure 2.5.
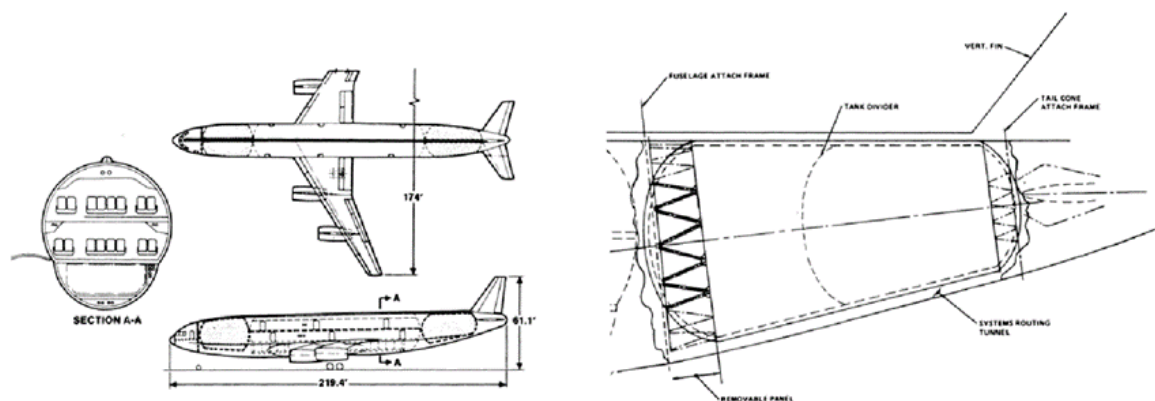
Figure 2.5: Blueprint of the aircraft and integral tank concept from Brewer [10]

Regarding thermal insulation, 15 candidate concepts were screened with 2 concepts selected and recommended for future investigations. These concepts consisted of a closed-cell polyurethane foam or microspheres contained in vacuum, with both options having an outer layer of open-cell flexible foam purged with gaseous nitrogen and a kevlar cover to provide mechanical protection and act as a vapor shield. This layer can be easily removed and replaced for maintenance or inspection, providing a critical advantage over a non-integral design [3]. In the second concept, a flexible stainless steel vacuum jacket is used to hold the vacuum.

Table 2.1 shows the results obtained by Brewer and the tank components included in the calculation of the FC mass. Note that the mass of the fuel system and additional vacuum pumps were also computed by this author but they are not part of the FC structure. It can be seen that both concepts have a similar performance and FC efficiencies of up to 0.78 can be obtained with this architecture.

However, the complexity of the truss system connecting the tank to the remaining airframe discouraged further research or a transition into practical applications. Moreover, Brewer raised concerns over the difficulty in fabrication and maintenance of the flexible steel jacket. Finally, the author suggests the addition of a small tunnel on top of the fuselage for systems routing, which would have an aerodynamic penalty that was not accounted for [3].

| | **Candidates** | | |
Item	**Foam**	**Vacuum**	**Units**
Tank and Body shell			
Stiffened wall mass	1303.9	1335.7	Kg
Tank divider mass	332.3	337.8	Kg
Truss system mass	838.1	845.3	Kg
Insulation			
Aero fairing mass	325.5	313.7	Kg
Vapor barrier mass	316.4	92.2	Kg
Open cell foam mass	246.1	238.8	Kg
closed cell foam mass	955.2	-	Kg
Microspheres mass	-	982.5	Kg
Vaccum jacket mass	-	417.2	Kg
FC mass	7926.4	8221.5	Kg
Fuel mass	27.326.3	27158.3	Kg
FC efficiency	0.78	0.77	Kg

Table 2.1: Summary of results obtained from Brewer for two candidate concepts [3]

2.2.3. Gomez and Smith Concept

The study by Gomez and Smith is the only investigation of an integral tank found in recent literature that sizes the tank according to the airframe loads and addresses the structural connections to the fuselage structure. In this study, a conventional mid-range aircraft design is converted to hydrogen by integrating large tanks in front and AFT of a shortened passenger cabin. An integral design is followed with a semi-monocoque structure stiffened with stringers and frames that are easily connected to the remaining fuselage structure, as shown in figure 2.6 [14].

Both tank structures are sized iteratively following EASA CS-25 air-worthiness specifications [35] and evaluating the stress concentrations via Finite Element (FE) analysis . Due to the inclusion of a catwalk in the FW tank, additional stiffeners are required to transfer the loads into the fuselage frame, increasing the structural mass of the tank. The aluminium alloy 2219 is selected for the tank structure, except for the area around the catwalk in which Al 7075 and Titanium are required to sustain the higher hoop stresses in this region.

The differentiating aspect of this concept is the use of internal insulation, more specifically inner wetted thermal insulation (IWTI) with metallic liners to reduce hydrogen permeation [36]. This insulation strategy provides two crucial advantages. First, it allows the tank structure to be radially aligned with the remaining fuselage structure as it would normally be displaced inwards by an amount equal to the insulation thickness. Second, the tank structure is maintained at almost ambient temperature avoiding heat conduction through frames and stringers and eliminating the challenge of managing the tank contraction and expansion at the connection with the airframe. However, as mentioned in subsection 2.1.1, the use of internal insulation in direct contact with hydrogen is a new technology
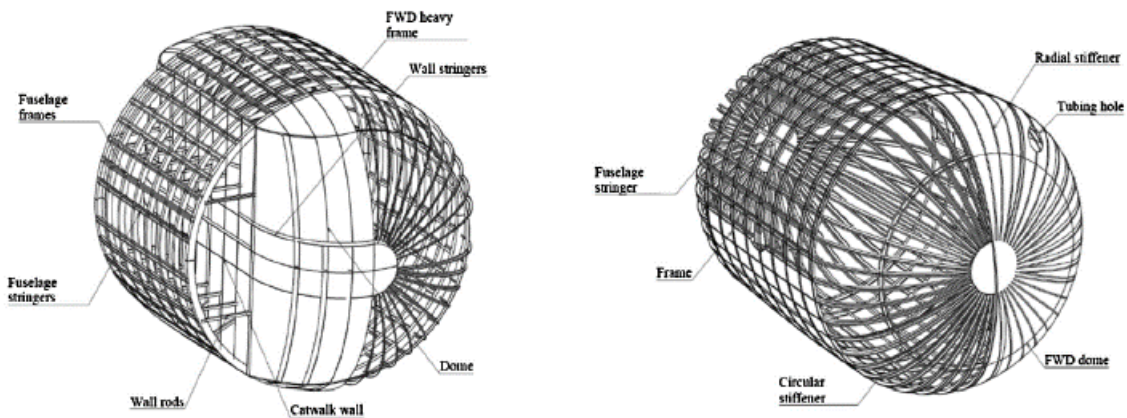
Figure 2.6: Structural arrangements of the integral tanks, by Gomez and Smith [14]

that is in development for space applications. Even with metallic liners, hydrogen permeation and foam embrittlement are issues that can not be answered by the current readiness level of this technology [21].

The FC efficiencies obtained with this concept were 0.83 for the AFT tank and 0.83 for the FWD tank, with the lower value justified by the presence of the catwalk. Despite the promising results, this concept relies on the success of unproven inner insulation, leading early hydrogen aircraft to use more conventional insulation designs, such as vacuum MLI.

2.3. PROPOSED SOLUTION

The previous analyses showed that existing integral tank concepts rely on single wall designs, compromising the integration with the airframe or the insulation capabilities of the tank. To address these issues, a new solution is proposed with a double wall construction and vacuum MLI insulation. Figure 2.7 shows a schematic representation of the tank design.

Although a double wall construction with vacuum insulation is not new in itself, it has not been applied to integral tank designs, due to the additional mass incurred. However, this architecture is not only required at current insulation technology levels, as explained in subsection 2.1.1, but also allows each vessel to be optimized for its respective function. The inner tank is responsible for holding the hydrogen and the loads associated with fuel containment, while the outer tank connects to the adjacent airframe and carries the loads of the primary structure. With the insulation in between, the outer tank structure can be directly bolted to the primary airframe avoiding issues with tank contraction/expansion and heat conduction through the structure. The mechanical connection between the outer and inner vessels is also represented. It is usually referred to as suspension as it handles the dimensional changes of the inner vessel, but a detailed design of this connection is beyond the scope of this proposal.
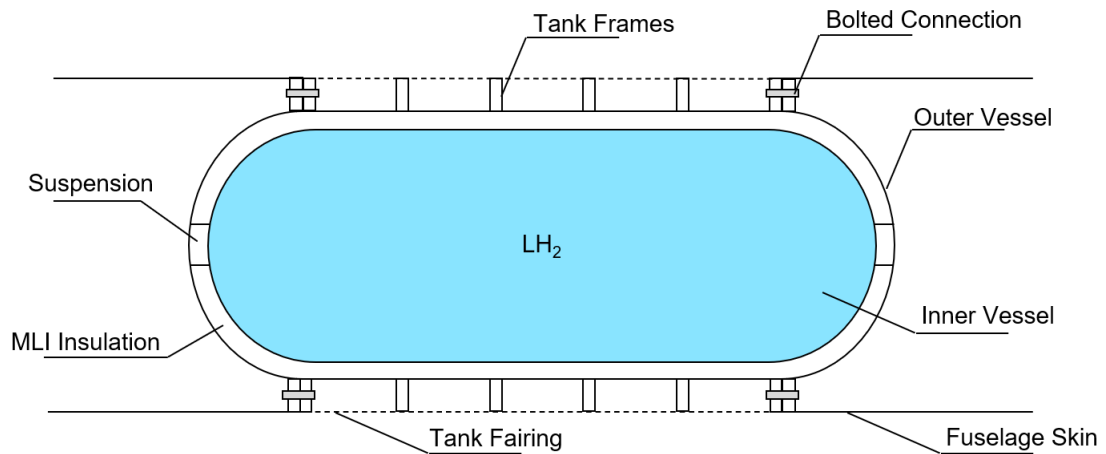
Figure 2.7: Integral tank concept with MLI insulation

Note that the tank structure utilizes frames and stringers on the outside, contrary to the concepts proposed by Brewer and Gomez. This configuration is not only safer for crash worthiness but also provides the necessary space for systems routing, avoiding the addition of exterior tunnels. A fairing is then attached to the frames to provide a smooth aerodynamic surface. Since it has no structural purposes, a kevlar layer with a thickness of 1.57×10^{-2} and density of $1.304 kg/m^3$ is used, derived from Brewer [2].

3

METHODOLOGY

In this chapter, the methodology proposed in this study is explained, starting with an overview of the main program structure in section section 3.1. Although the focus of this work is on detailed tank sizing, the sizing loads were not directly available from literature and therefore had to be estimated. Hence, this framework includes the process to integrate the tank in the fuselage and calculate the sizing loads, which are described in sections 3.2 and 3.3. In the remaining sections, the tank sizing is described in detail, covering the FE modeling and the mathematical formulation of the optimization problem.

3.1. PROGRAM STRUCTURE AND MODEL INPUTS

Figure 3.1 gives an overview of the workflow developed in this research, divided into its two main parts.
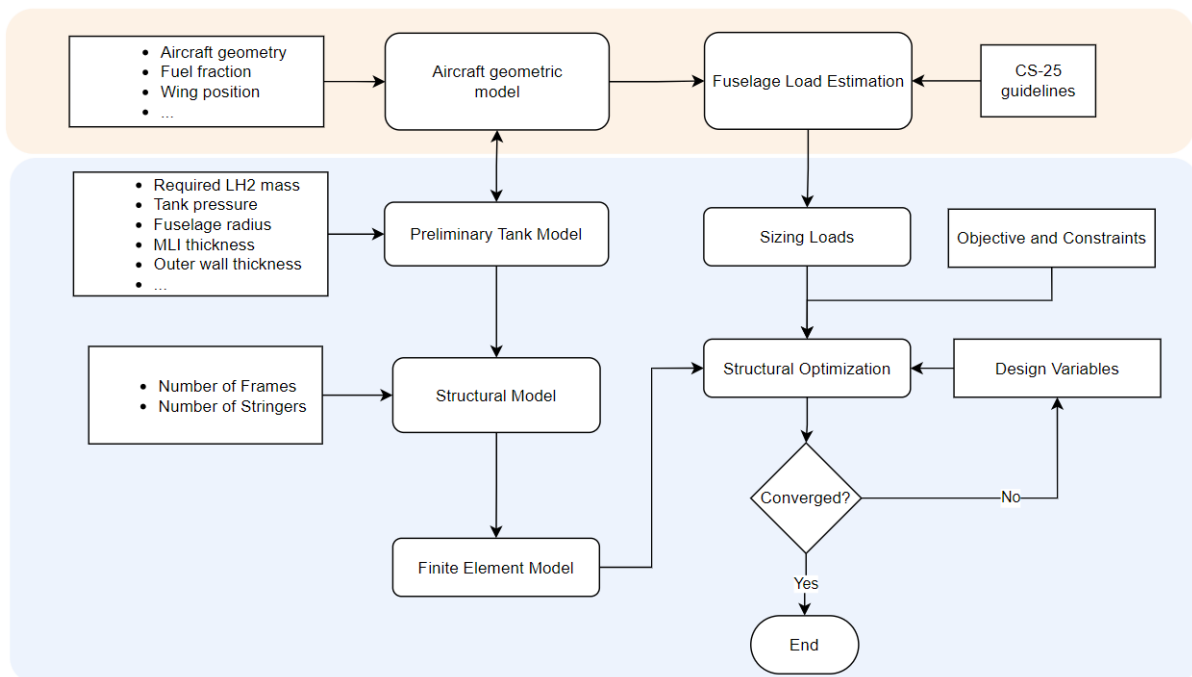
Figure 3.1: Program structure of the detailed tank sizing

The first phase represents a more comprehensive aircraft design tool that would perform multi-disciplinary analyses to integrate the hydrogen tanks and update the load distribution accordingly. This research builds on previous studies by using the aircraft geometry generated from such analyses as a platform to calculate the loads. One geometric parameter of particular importance is the wing-shift. Since the addition of hydrogen tanks changes the mass distribution of the aircraft, the wing must be repositioned to ensure that control and stability requirements can be met by the new configuration. Consideration of this and other factors, such as updated aerodynamic surface areas, adds to the quality of the research and further justifies the use of this data.

Based on the generated aircraft model, the mass of individual components is obtained using class-II estimations. Subsequently, the method computes the the loads acting on the fuselage following CS-25 guidelines for fuselage compliance. Then, the internal fuselage loads are determined from beam theory and the loads at the tank location are extracted for the structural analysis.

In the second and most important part of the methodology, the structure of the thank is sized to handle the loads obtained in the previous section. A FE analysis can be used to compute the response of the structure under the applied loads and constraints but in order to size the structure, it must be incorporated into a sizing routine. As depicted in figure 3.1, this routine can operate as an sub-discipline to the multidisciplinary aircraft design loop, taking as inputs the fuselage loads at the tank location and the required fuel mass, calculated in a mission analysis discipline. First, a structural model is built based on the preliminary tank dimensions. Here, simplifying assumptions are used to represent represent the crucial elements of the tank structure such as the frames and stringers, reducing the computational cost of the analysis. Next, a mesh is created to discretize the model into individual elements.

The optimization problem is then formulated in the form of a structural mass minimization. This formulation considers specific design criteria to size the structural elements, which is given as constraints on the strength, buckling stability and fatigue behaviour. Also, specific geometric parameters related to the dimension of the structural elements are assigned as design variables and allowed to change within a specified range. The computational cost associated with this form of structural optimization is considerably less than a full topology optimization and therefore is a suitable choice for this thesis. Finally, an input file for NASTRAN is generated and a structural optimization is performed, iterating the design variables until the solution with the minimum mass that meets the constraints is found. It is worth noting that NASTRAN uses a gradient based method that relies on design sensitivities to find the best search direction. Thus, there is a risk of terminating the analysis at a local minimum and overlooking further mass savings. Such a risk can be mitigated by choosing appropriate initial values for the design variables. As a semi-monocoque wall design is used, the reference dimensions of the fuselage airframe are selected, as it is expected that the optimum design will be close.

To efficiently generate and analyze different structural designs, a Knowledge Based Engineering (KBE) is applied, automating the repetitive task mentioned above. Among the available tools, the ParaPy platform was selected for this research project due to its capabilities of building complex models based on the principles of KBE and Object-oriented Programming (OOP). A similar approach was used by Nanninga to estimate the structural weight of the outer wing of the Flying-V [37].

In addition to assigning initial values to the design variables, various parameters must be defined or assumed in order to size the tank structure. These parameters are fixed during the optimization process and therefore, are designed as 'fixed inputs'. Unless otherwise specified, the values were retrieved from Onorato for consistency [16]. A brief description of each input is provided below:

- Required hydrogen mass: top level requirement which must come from a mission analysis discipline or be provided by the user. It concerns of the total fuel mass required for the mission, including vented and unused fuel. This input is directly used in the calculation of the FC efficiency η_{FC}.

- Density of liquid hydrogen of 71 kg/m^3

- Tank ullage and volume allowances: The first is necessary to avoid pressurization of the tank, particularly at the airport during holding times. Common values suggested are between 2% and 5%, with the former being used here. The second is required to account for trapped fuel, tank contraction and internal equipment, which add up to 3% [3]. Both inputs increase the tank volume required for a given hydrogen mass.

- Fuel fraction: determines the distribution of hydrogen fuel between the AFT and the FWD tanks. Both 0 and 0.6 are used, depending on the aircraft layout being studied

- Dome ratio: defined as the ratio between the tank radius and the dome length. Ratios between 1 and 2 can be selected, with the first corresponding to a spherical dome. A baseline value of 1.6 was selected, as Brewer determined this shape would result in the lowest operating cost [3].

- Sizing loads, which are discrete values of external pressure, bending moment and shear force resulting from the critical load cases

- Maximum Operating Pressure (MOP) of the hydrogen fuel inside the tank, which must be above atmospheric. A baseline value of 250 kPa was selected.

- Fuselage radius and frame height of 1.99 m and 0.120 m, retrieved from [38], for an A320.

- Material properties of both aluminium alloys, provided later in this chapter

- Fatigue concentration factor of 4.5

- Thickness of MLI insulation of 30 mm, retrieved from [39], and density of 45.0kg/m^3, assuming 40 layers per centimeter [40]

- Thickness of outer fairing of 1.57 mm and density of 1.304kg/m^3, given by Brewer [2]

- Number of stringers and frames, as well as the shape of each stiffener.

- Number of mesh elements between stringers: dictates the minimum size of the mesh elements and is defined after a mesh convergence study

To increase the robustness of the framework and establish design trends, some of the parameters above were selected for additional analyses, including a design of experiments (DOE) to determine the optimum structural layout in terms of frame height, number of frames and stringers. Also, sensitivity studies were performed on the dome shape, stringer shape, fatigue concentration factor, MOP and MLI thickness.

3.2. AIRCRAFT INTEGRATION AND TANK GEOMETRY

The geometric aircraft models are built based on the reference data from Onorato. If the required hydrogen mass is zero or not specified, a baseline model is generated, corresponding to the existing kerosene aircraft. Otherwise, an hydrogen aircraft is created, with the tank layout depending on the fuel fraction specified. For a fuel fraction equal to one, a single AFT tank is positioned behind the cabin. For fuel fractions lower than unity, an additional tank is positioned in front of the passenger cabin. As previously outlined in section 2, this option is typically required in larger aircraft to reduce the shift in CG [24]. Due to the position of the FWD tank, it is always non-integral, leaving a small passage for passengers and crew. For this reason, the detailed tank sizing is applied exclusively to the AFT tank.

In accordance with the approach from Onorato, the radius of the fuselage is kept constant and its length is increased to accommodate the hydrogen tanks, thereby maintaining the passenger capacity of the baseline aircraft [16]. Although a fuselage extension may impact airport operations, it is not a new approach within the aviation industry. As an example, similar modifications are implemented to obtain an Airbus A350-1000 from the baseline A350-900. Furthermore, this strategy was preferred over one in which the passenger capacity was reduced given that the longer fuselage will result in higher bending and shear forces on the fuselage, leading to a more conservative design. A schematic image of the three configurations is shown in figure 3.2.
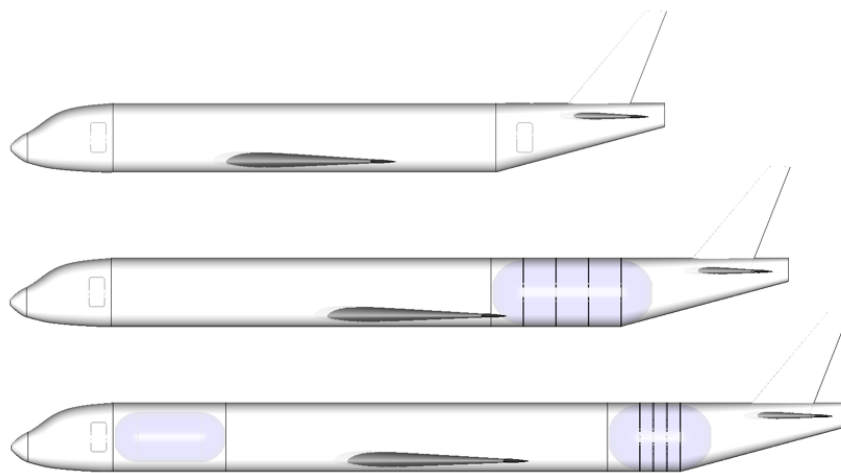
Figure 3.2: Baseline aircraft and hydrogen variants, generated in Parapy

The preliminary tank geometry consists of two shells, defining the inner and outer tank walls. Following a KBE approach, geometric parameters are defined in order to quickly generate different tank designs. The parameterization by Winnefeld is the reference commonly used in literature for spherical and cylindrical tanks [12]. While these shapes would generally be sufficient for tanks in the fuselage, it is desirable to have a parameterization capable of studying conical tanks and elliptical cross sections, allowing the research to be extended in the future. To this end, the parameterization proposed by Silberhorn and shown in figure 3.3 offers more flexibility and will therefore be used in this work but limited to cylindrical shapes ($Z_{offset} = 0$, $a = b$)[9]. The shape of the domes can be defined by selecting the ratio between the the tank radius and the dome length as mentioned before.
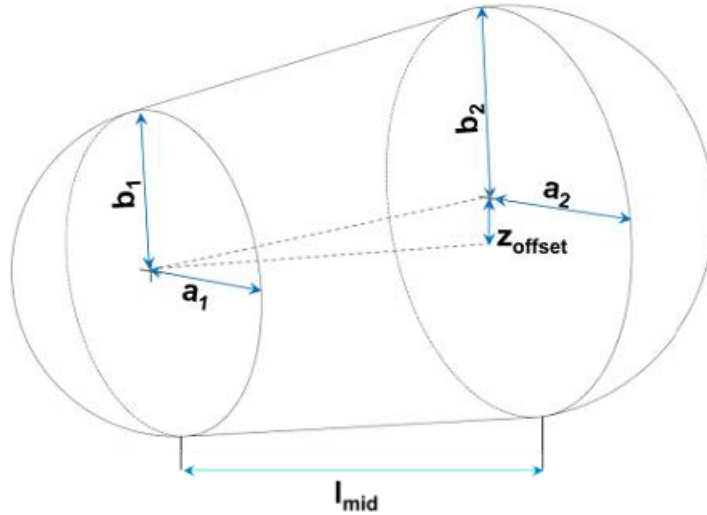
Figure 3.3: Tank geometric parameters, extracted from [9]

The main dimensions of the tank are calculated with an outside-in approach, based on the required hydrogen mass. Figure 3.4 gives a detailed representation of the geometric parameters considered. First, the radius of the inner tank is determined based on the values defined for the protective fairing (t_f), frame height (h_{fr}), outer shell thickness (t_{sk_o}), insulation thickness (t_{ins}) and inner shell thickness (t_{sk_i}). As the focus of the research is on the sizing of the outer shell, the thickness used here is an initial guess. The tank length is then calculated based on the volume required to carry the specified fuel volume, while accounting for ullage and other allowances.
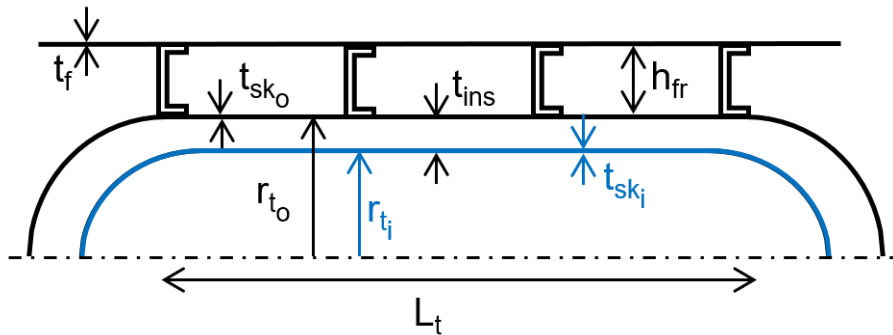
Figure 3.4: Tank geometry in preliminary sizing

For preliminary sizing of the inner vessel, most studies consider only internal pressure loads related to the fuel containment. In that case, the tank wall thickness can be determined from the hoop stresses on the skin, according to equation 3.1. Here, the expression was simplified by assuming an ideal vacuum between both tanks, which is reasonable assumption as MLI requires a vacuum pressure below 10^{-4} torr to be effective [11]. However, this computation is expected to underestimate the required wall thickness, as it does not take into account the hydrostatic pressure increments due to aircraft accelerations or the thermal loads due to the cryogenic fuel. In the present research, these effects are captured by an increased safety factor, as done in [41]. Comparing the results obtained with equation 3.1 with a more complete study which considered thermal loads, a 3.5g vertical acceleration and a 0.5g lateral acceleration, the authors found that a safety factor of 2.4 would be more appropriate.

A 2219-T851 aluminium alloy was selected for the inner tank, as according to Brewer, it provides "ductility at cryogenic temperatures as well as weldability, stress corrosion resistance, high fracture toughness, and resistance to flaw growth." [2]. Also, Brewer determined a fatigue stress of 172 MPa considering 40000 cycles, which is the value used in the sizing. The same wall thickness is used for the domes, which is a sensible option to reduce the manufacturing costs.

$$t_{sk} = \frac{SF.Pr}{\sigma_{Hoop}} \tag{3.1}$$

3.3. LOAD CASES

Since it is impractical to predict or study all the loading conditions that an aircraft is subjected to during its lifetime, airworthiness authorities have set technical specifications and requirements to ensure the structural integrity of any aircraft. In Europe, the current legislation for large aeroplanes is the European Aviation Safety Agency (EASA) Certification Specifications for Large Aeroplanes (CS-25). As the study concerns tanks integrated into the fuselage structure, four main sources of loads are considered, in accordance with CS-25 guidelines for fuselage compliance[35]: weight loads, pressure loads, aerodynamic loads and ground loads. Figure 3.5 shows how the loads are applied to the aircraft. The fuselage is assumed to be supported at the wing spars, which transmit the vertical forces from the wing and main landing gear.
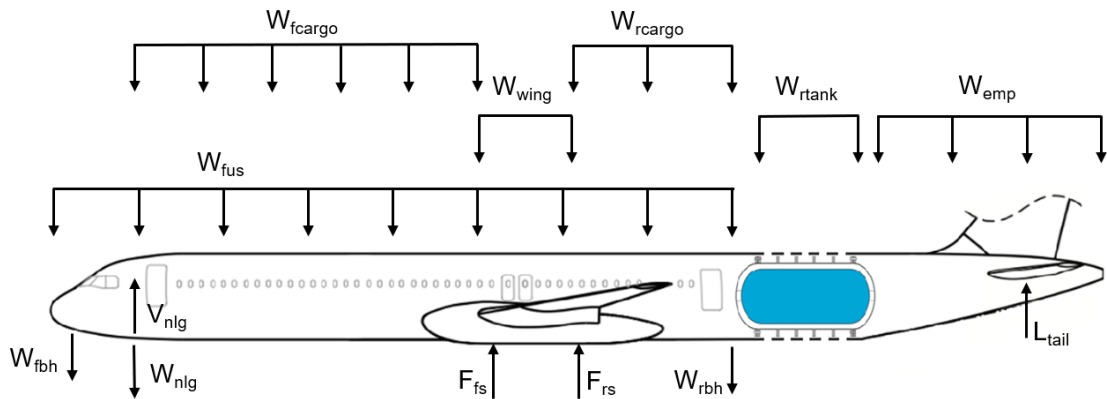
Figure 3.5: Forces acting on the aircraft, adapted from [42]

Load cases are defined to provide realistic combinations of the individual load sources. The selected cases are listed in table 3.1. For all cases, MTOM is considered, in a conservative approach.

Load Case	Description	Load Factor	Mass	Pressure
LC1	Steady Flight	1G	MTOM	$1.33\Delta p$
LC2	Pull-up manoeuvre	2.5G	MTOM	$1.33\Delta p$
LC3	Pull-down manoeuvre	-1G	MTOM	$1.33\Delta p$
LC4	Lateral Gust	1G	MTOM	$1.33\Delta p$
LC5	Engine out	1G	MTOM	$1.33\Delta p$
LC6	3 Point Landing	-2G	MTOM	$1.33\Delta p$

Table 3.1: Load cases

3.3.1. WEIGHT AND BALANCE

Weight loads result from the gravitational force acting on the mass of each component. Torenbeek provides a method to divide the aircraft into individual groups and estimate the mass of each group using empirical relations. As shown in figure 3.5, the weight of all groups is applied as a distributed load over the corresponding length, except for the weight of the nose landing gear and pressure bulkheads, which are applied as point loads. Table 3.2 provides an overview of the components included in each group, with a more comprehensive description available in [42]. In the following subsections, just the contributions specific to the hydrogen aircraft will be covered.

Weight Group	Components
Fuselage (W_{fus})	Airframe structure, equipment and services, furnishing, paint
Wing (W_{wing})	Wing, wing box, propulsion system, main landing gear
Empennage (W_{emp})	Horizontal tail, vertical tail, empennage structure, APU
Front cargo (W_{fcargo})	Front cargo floor, front cargo handling
Rear cargo (W_{rcargo})	Rear cargo floor, Rear cargo handling
Rear Tank (W_{tank})	Tank structure and insulation

Table 3.2: Weight Distribution

HYDROGEN TANK MASS

The total tank mass is the mass related to the fuel containment and is obtained by adding the individual contributions related to the tank insulation and structure, including the tank fairing, external shell and internal shell. Each contribution is automatically calculated in Parapy, using the correspondent volumes and defined material densities. Note that obtaining an accurate estimation of the external wall mass is the focus of this research. To already account for the stiffeners in the preliminary tank sizing, an empirical rule from Torenbeek is adopted. According to this author, the mass of the stringers can be assumed to be equal to 50% of the skin and the weight of frames to be equal to 20% of the stiffened skin weight [43].

Finally, there are additional components that should be included for a conservative mass estimation. Onorato computed the mass of a tank divider, assuming it would have a similar mass to the end caps of the tank as they follow a similar construction. This results in a value around 100 kg for the aircraft considered [16]. Additionally, Brewer suggested that an allowance of 8% should be used to account for manufacturing tolerances, joints and support of fuel related operating systems such as pumps, valves and sensors. It i assumed that the mechanical connection between the inner and outer tank is included here and both values were adopted in this research, to reach a conservative design. The final mass is given by equation 3.2:

$$m_{FC} = 1.08(m_f + m_{wall,i} + m_{wall,o} + m_{ins} + m_{div}) \tag{3.2}$$

HYDROGEN FUEL SYSTEM WEIGHT

The fuel system mass of a conventional kerosene aircraft can be estimated with Equation 3.3, from Torenbeek which takes into account the number of engines (N_e), number of fuel tanks (N_{ft}) and fuel tank volume (V_{ft}) [44].

$$m_{fuelSys} = 36.3.(N_e + N_{ft} - 1) + 4.366.N_{ft}^{0.5}.V_{ft}^{0.333} \tag{3.3}$$

However, due to the complexity of handling cryogenic fuel and the location of the tanks, hydrogen fuel systems are expected to be heavier. Using the detailed design of a liquid hydrogen fuel system

by Brewer as a reference, Onorato proposed the use of a correction factor of 2. This factor was then validated with the results from Silberhorn et al, resulting in a minor discrepancy of approximately 2% [16].

3.3.2. PRESSURE LOADS

Pressure loads stem from the use of vacuum insulation, which subjects the outer shell to an external pressure force. Applying CS-25 guidelines for pressurized fuselages to hydrogen tanks, the tank structure is sized to withstand 1.33 times the pressure differential, with a safety factor of 1.5 [35]. The pressure differential acting on the external wall is given by equation 3.4. As done for the inner wall, the vacuum pressure is assumed to be negligible.

$$\Delta p = P_{out} - P_{vaccum} \approx P_{out} \tag{3.4}$$

Where P_{out} refers to the pressure outside the tank. For ground cases, the pressure is taken at sea level, with a value of 101325 Pa. For the manoeuvre cases, the pressure is taken at cruising altitude. This formulation considers that the tank is located in an unpressurized section of the fuselage, as this is the safest approach according to Huete [27]. Moreover, integrating the tank in a pressurized section of the fuselage would add complexity to the design, as the outer fairing, which currently has no structural role, would also be subject to a pressure differential.

3.3.3. AERODYNAMIC LOADS

Aerodynamic loads are evaluated for limit symmetrical manoeuvring conditions at the corners of the flight envelope, in accordance with figure 3.6. Limit loads represent the maximum loads that the aircraft is expected to encounter during normal operation and no permanent deformation is allowed in the structure up to these loads. Specifically, load factors of 2.5 and -1 are evaluated at the design cruising speed, as required in CS-25 regulations [35]. Ultimate loads are not considered in this research as they are expected to permanently deform and damage the airframe. Hence, an analysis of these loads would entail a study in the plastic range of the material, which is beyond the scope of this work. Additionally, to ensure proper sizing of the tank's side panels, lateral cases are also considered, corresponding to loads on the vertical tail caused by lateral gusts or side-slipping flight.
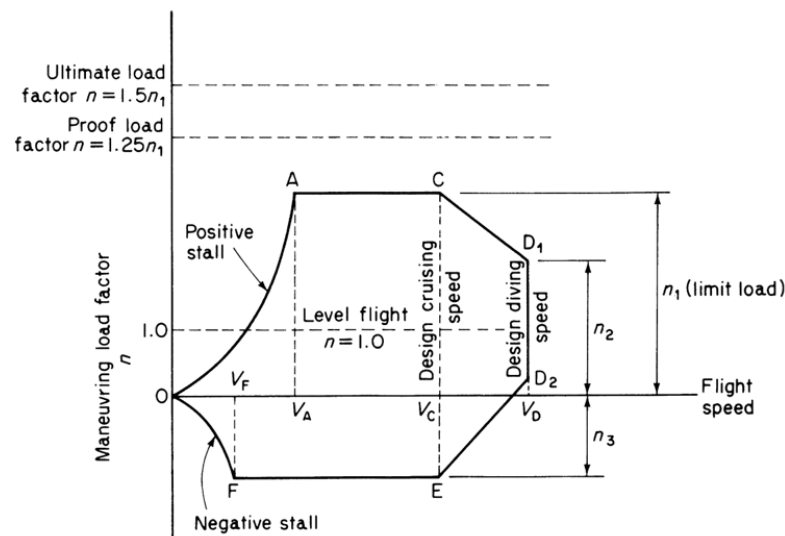
Figure 3.6: General flight envelope, retrieved from [45]

SYMMETRIC MANOEUVRE

In a preliminary approach, the concept of load factor can be used to reduce the dynamic flight conditions to a static equilibrium. Following the diagram of figure 3.7 the general vertical equilibrium of forces is given in equation 3.5, where both the wing lift and the tail lift are modelled as concentrated forces acting on the aerodynamic center of the respective surface.
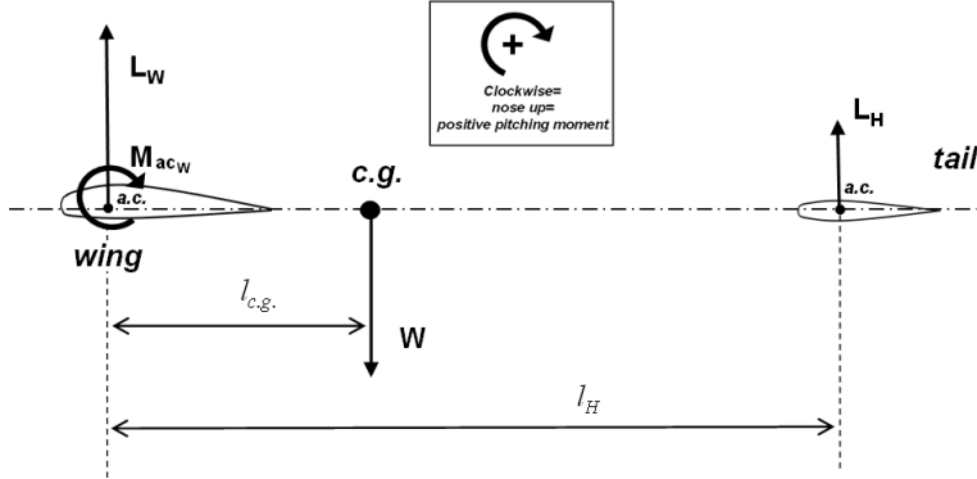
Figure 3.7: Simplified aircraft geometry for load calculation

$$\sum (F_z) = 0 : L_w + L_{ht} = n_z.W \tag{3.5}$$

Taking moments around the CG,

$$\sum (M_{cg}) = 0 : M_{ac_w} + L_w.l_{cg} - L_{ht}.(l_{ht} - l_{cg}) \tag{3.6}$$

Considering L as total lift ($L_w + L_{ht}$), equation 3.6 can be simplified to:

$$M = M_{ac_w} + L.l_{cg} - L_{ht}.l_{ht} \tag{3.7}$$

In dimensionless form:

$$C_M = C_{M_{ac_w}} + C_L.\frac{l_{cg}}{c} - C_{L_{ht}}.\frac{S_{ht}.l_{ht}}{S.c} \tag{3.8}$$

Employing the following relations:

$$C_L = \frac{n_z.W}{q.S_w} \tag{3.9}$$

$$V_{ht} = \frac{S_{ht}.l_{ht}}{S.c} \tag{3.10}$$

$$C_{L_{ht}} = \frac{C_{M_{ac_w}} + C_L.\frac{l_{cg}}{c}}{V_{ht}} \tag{3.11}$$

Finally, the balancing tail load is calculated:

$$L_{ht} = q.S_{ht}.C_{L_{ht}} \tag{3.12}$$

Equations 3.5 and 3.12 are used to calculate the aerodynamic loads for each load case, based on the load factor n_z. It should be noted that the impact of gusts on the load factor was not considered, as they are typically not critical in a symmetric manoeuvre. Furthermore, the following simplifying assumptions were employed:

- Pitching acceleration is assumed to be negligible and airspeed, mach and altitude remain constant during the manoeuvre

- Lift forces are assumed to be equal to the normal forces

- Drag and thrust contributions to bending moment are assumed to be negligible. This assumption may not be valid in T-tail configurations

- Horizontal tail pitching moment is neglected as it is small when compared to the wing

LATERAL GUST

The lateral gust load is modelled as a concentrated force acting on the vertical tail and is computed according to equation 3.13 [46].

$$L_{vt} = k_g \frac{1}{2} \rho_0 U_E V_E S_{vt} C_{L_{vt}\beta} \tag{3.13}$$

Where U_E is the equivalent gust velocity, V_E is the equivalent airspeed, S_v is the reference area of the vertical tail and $C_{L_v\beta}$ is the lift coefficient derivative with respect to the side slip angle β. These parameters are calculated with the relations described in [42].

ENGINE OUT

A flight condition with an engine failure often proves to be critical for the sizing of the AFT fuselage, as large bending moments are created due to the asymmetric thrust. In order to control the aircraft, a rudder input is required. Equations 3.14 and 3.15 calculate the required force on the vertical tail from the moment equilibrium around the CG.

$$\sum(M_{cg}) = 0 : 0 = T.y_{eng} - L_{vt}.cos\beta(l_{vt} - l_{cg}) \tag{3.14}$$

$$L_{vt} = \frac{T.y_{eng}}{cos\beta(l_{vt} - l_{cg})} \tag{3.15}$$

3.3.4. GROUND LOADS

In this research, ground loads are limited to landing cases, which introduce high vertical forces in the fuselage. In particular, a three-point landing, in which the nose and the main gears contact the runway simultaneously. Given that a two-point landing typically has load factors below 2.5 and the loads of the main landing gear are transferred to the fuselage through the wingspars, this case can be assumed to be covered by the symmetric manoeuvre load.

THREE-POINT LEVEL LANDING

A simplistic rigid body analysis derived from Lomax [46] is used to compute the loads, reducing the highly dynamic case to a static problem. This approach is in line with the preliminary scope of this research and does not require a detailed knowledge of the landing gear and shock absorption system.

From the force equilibrium in the vertical direction according to figure 3.8,

$$\sum(F_z) = 0 : V_{NG} + V_{MG} = n_z W - L \tag{3.16}$$
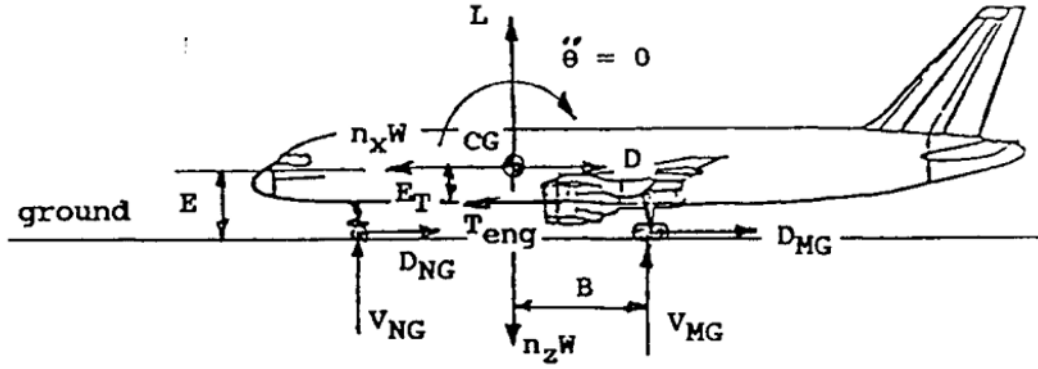
Figure 3.8: Three-point landing condition, extracted from Lomax [46]

Since $L = W$ by CS-25 definition [35],

$$V_{NG} = W(n_z - 1) - V_{MG} \tag{3.17}$$

Making the assumption that the pitching moment is resisted by the nose gear and that the contributions of thrust and drag can be neglected, the ground reaction force becomes:

$$V_{NG} = (n_L - 1)W\frac{F}{1+F} \tag{3.18}$$

$$F = \frac{A + 0.25e_M}{B - 0.25e_N} \tag{3.19}$$

Where n_L is the landing load factor, W is the weight of the aircraft, A is the horizontal distance between nose landing gear and center of gravity, B is the horizontal distance between main landing gear and center of gravity. Further, $e_M = hcg - r_M$ and $e_N = h_{cg} - r_N$, with h_{cg} being the height of center of gravity, r_{MG} the main gear wheel rolling radius and r_{NG} the nose gear wheel rolling radius.

3.3.5. RUNNING LOADS

Based on the loads calculated, the distribution of bending moment and shear force across the fuselage can be determined from beam theory. In this approach, the fuselage is sliced at in incrementally larger sections, as shown in figure 3.9, and at each section the internal fuselage loads that satisfy the static equilibrium are computed. Finally, the maximum loads at the tank location are extracted and used for the structural analysis.
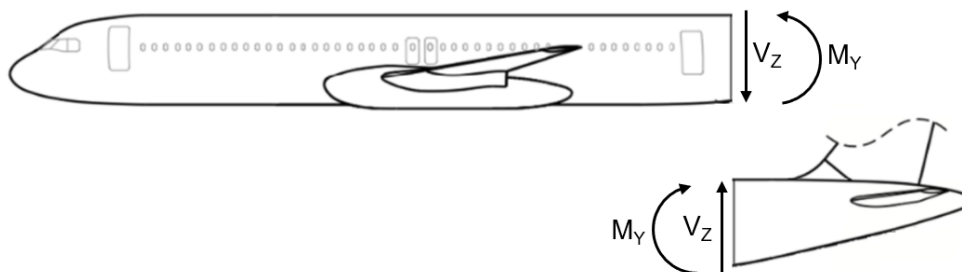
Figure 3.9: Sign convention of bending moment and shear force

3.4. FINITE ELEMENT MODEL

In a finite element analysis, it is often not practical to include all the geometric features of the structure. Therefore, the structure is idealized into a physical model to allow the analysis to take place. The accuracy of the results is closely linked with the ability of the model to represent the real structure. This section will provide an overview of the structural idealization in subsection 3.4.1, which sets the basis for the meshing process, described in subsection 3.4.2.

3.4.1. STRUCTURAL MODEL

The structural model adopted in this research represents the external tank wall and consists of a stiffened cylindrical shell, closed by domes. As shown in figure 3.10a, stringers are evenly distributed around the tank based on the total number of stringers defined (which can be manually changed by the user). Similarly, frames are equally spaced based on the number of frames defined, with the fir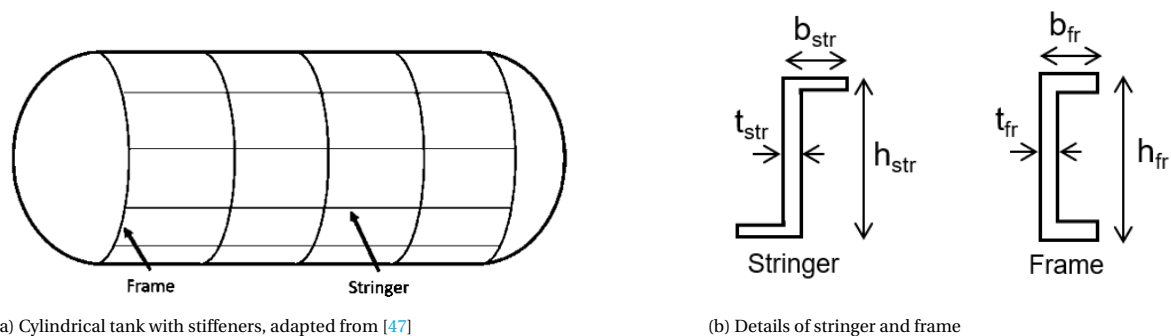st and last frames always positioned at the ends of the cylindrical section of the tank. The connections between the different structural elements are not explicitly modeled in this idealization, which is in line with the preliminary approach of the thesis.

(a) Cylindrical tank with stiffeners, adapted from [47]   (b) Details of stringer and frame

Figure 3.10: Structural tank model

Thin structures such as the tank skin are well represented by 2-dimensional geometries, defined at the mid-surface of the component. This approximation is valid when the thickness of the skin is much smaller than its other dimensions, making the stress developed in the thickness direction negligible. Frames and stringers are also reduced to 1-dimensional edges, as their length dimension is much larger than the other two. These edges are generated by defining planes at the locations of the stiffeners and intersecting those planes with the skin surface.

The foregoing approximations reduce the computational cost of the analysis without compromising its accuracy. NASTRAN accomplishes this by completing the geometric definition of the elements in a physical property table. The table for a 2-dimensional shell stores its thickness dimension while the table for the 1-dimensional beams stores the properties of the stiffener's cross section. Figure 3.10b details the cross section geometry of the stiffeners, considering, Z-stringers and C-frames. During pre-processing of the analysis, the user can select different shapes such as HAT-stringers or I-frames. For all cases, two simplifying assumptions are used. First, the thickness is considered to be constant over the flanges of the stiffeners. Second, the height of both stiffeners (h) is considered to be twice their width (b).

3.4.2. Meshing

With the geometry created, the model can be discretized into elements which are connected together to form a mesh. The purpose of the discretization is to solve the equilibrium requirement over a finite number of elements, instead of continuously over the entire structure. Notwithstanding the simplifications of the structural model, various surface and line elements can still be selected, with an impact on the accuracy and computational cost of the analysis

In this work, shell elements are used to model the tank skin, which are capable of capturing both in plane and bending stresses, based on Kirchhoff theory [48]. In particular, NASTRAN rectangular element (CQUAD4) are preferred to triangular (CTRIA3) as the latter are elements of constant deformation and strain. For the stiffeners, rather than using bar elements which can only carry axial loads, beam elements corresponding to NASTRAN PBEAML entries are used, as they can carry axial, bending, shear and torsional loads. To ensure element connectivity, line elements use the same mesh nodes as the skin. However, a section offset must be introduced to account for the stiffener position relative to the skin. Also, the offset must be updated at every iteration of the sizing process to account for changes in the geometric properties of the skin and stiffeners, which is accomplished in NASTRAN using DRESP2 entries.

The meshing strategy described generates an orthogrid mesh, allowing the number and size of elements to be controlled by selecting the number of elements between stiffening elements. As the aspect ratio of the QUAD elements should be close to unity for a high quality mesh, a rule was put in place to automatically compute the number of elements between frames based on the number of stiffeners and number of elements between stringers. This rule is based on figure 3.11 and derived in equations 3.20 and 3.21.
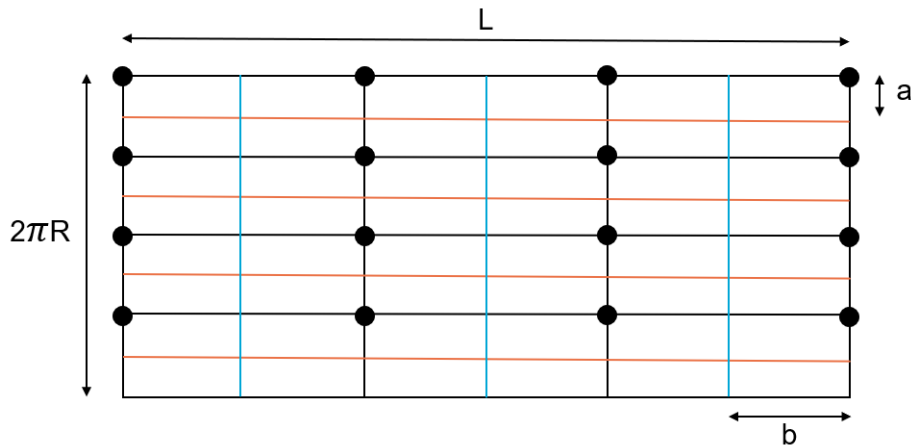
Figure 3.11: Meshing rule for an orthogrid structure

$$a = \frac{2\pi R}{n_{str} n_{circ}} \quad and \quad b = \frac{L}{(n_{fr} - 1) n_{long}} \tag{3.20}$$

Where R and L are respectively the radius and length of the cylindrical cross section, n_{str} is the number of stringers, n_{fr} is the number of frames, n_{circ} is the number of mesh elements between stringers and n_{long} is the number of mesh elements between frames. Imposing equality between a and b results in the following expression for n_{long}:

$$n_{long} = n_{str} n_{circ} \frac{L}{2\pi R(n_{fr} - 1)} \tag{3.21}$$

In this manner, for a given structure with a defined number of stringers and frames, a single parameter (n_{circ}) is required for mesh control and refinement. In section chapter 4, a mesh refinement study is carried to evaluate the impact of this parameter on the results and determine the minimum number of elements that still represents the geometry and produces accurate results.

The meshing process is totally automated in Parapy, to generate a high-quality quality mesh for different combinations of the input parameters. The result is depicted in figure 3.12, with the complete mesh on the left, along with the shell and beam elements.
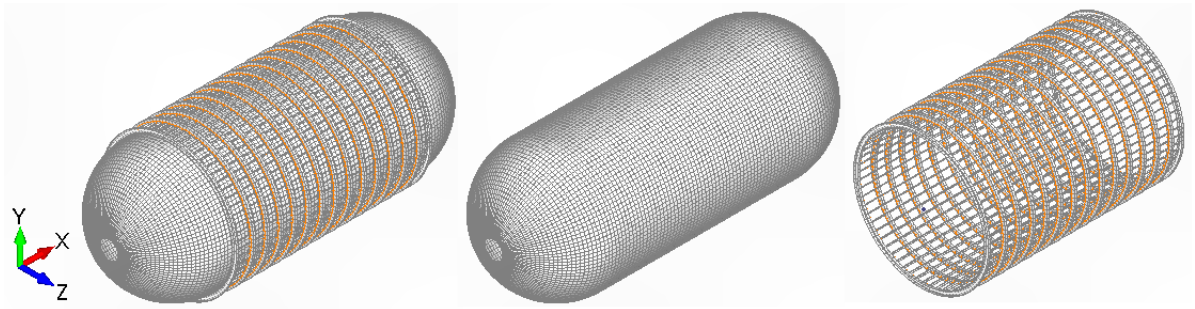
Figure 3.12: Complete Mesh

3.4.3. MATERIALS

As mentioned before, the analysis in this thesis is limited to common aluminium alloys used in aviation. For the outer tank, 2024-T351 aluminium alloy was adopted based on the data available on its fatigue behaviour, derived from Rubiaie [49]. Assuming that all deformations take place in the elastic range of the material, it is modelled in the software as linear elastic according to the properties from table 3.3.

Property	Symbol	Value	Units
Young's Modulus	E	73.1	GPa
Poisson's ratio	ν	0.3	-
Density	ρ	2780	Kg/m^3
Tensile Yield stress	σ_y	324	MPa
Compressive buckling constant	K_σ	5.35	-
Shear Buckling Constant	K_τ	4	-

Table 3.3: Material properties of 2024-T351 aluminium alloy

3.4.4. MODEL LOADS

The external tank wall is subjected to external pressure, bending moment and shear force. Figure 3.13 shows how the loads are applied to the finite element model. One significant simplification in the approach is the omission of loads in the connection with the inner vessel, which would arise from aircraft accelerations. It is expected that a structural reinforcement in the domes would be required to support these loads, motivating their inclusion in a detailed design phase.
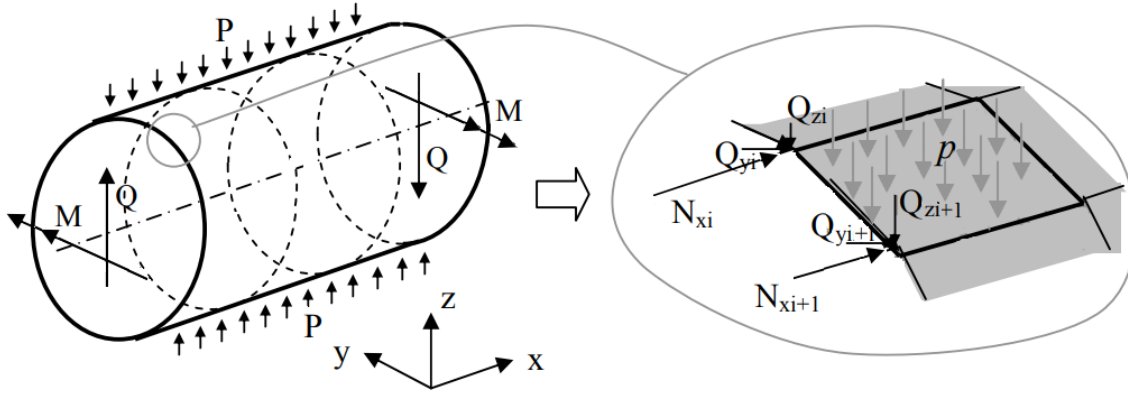
Figure 3.13: Load application on the FE model, adapted from [38]

The pressure load is applied at the center of each skin element, ensuring that the direction of the pressure field points inwards. The bending moment and shear force are transformed into equivalent nodal loads and applied at both ends of the tank's cylindrical section. Axial loads with a magnitude proportional to the distance to the neutral line produce the bending moment while, circumferential loads represent the shear flow over the cross section. This section provides the derivation of the equivalent nodal loads. In chapter 4, a test tank is used to validate the load application and evaluate the structural response to each load.

BENDING MOMENT

In the most general form, the normal stress due to bending moment is given by:

$$\sigma_x = \frac{(M_y I_{zz} - M_z I_{yz})z - (M_z I_{yy} - M_y I_{yz})y}{I_{yy} I_{zz} - I_{yz}^2} \tag{3.22}$$

Since yz-axis are axis of symmetry ($I_{yz} = 0$), equation 3.22 can be simplified to:

$$\sigma_x = \frac{M_y z}{I_{yy}} - \frac{M_z y}{I_{zz}} \tag{3.23}$$

Note the negative sign on M_z, which is introduced to account for the coordinate system sign convention. Then, the axial load at each node can be computed with equation 3.24

$$N_{x_i} = \sigma_{x_i} * A_i \tag{3.24}$$

Following the approach used in [38], different expressions are derived for nodal loads at stringer locations and in between stringers, with the former accounting for the contribution of the neighbouring skin panels. The total axial load at each node is given by equations 3.25 and 3.26, considering the same material for both stringers and skin.

$$N_{xi} = (\frac{M_y R \cos\theta_i}{I_{yy}} + \frac{M_z R \sin\theta_i}{I_{zz}})(A_{str_i} + \frac{1}{2}A_{sk_{left}} + \frac{1}{2}A_{sk_{right}}), \qquad \text{at stringer locations} \qquad (3.25)$$

$$N_{xi} = (\frac{M_y R \cos\theta_i}{I_{yy}} + \frac{M_z R \sin\theta_i}{I_{zz}})(\frac{1}{2}A_{sk_{left}} + \frac{1}{2}A_{sk_{right}}), \qquad \text{between stringer locations} \qquad (3.26)$$

SHEAR FORCE

The equivalent shear forces are derived from the shear flow on the cross section of the tank. As the stringers cause discontinuities in the shear flow, an equivalent thickness $\bar{t}$ is considered, with the stringers smeared over the skin.

$$\bar{t} = t_{sk} + \frac{n_{str} A_{str}}{shell \ length} = t_{sk} + \frac{A_{str}}{b_{str}} \qquad (3.27)$$

where b_{str} is the spacing between stringers. Using the equivalent thickness, the shear flow is given by:

$$q_s = -\frac{V_z}{I_{yy}} \int_0^s t_{sk} y(s) \, ds \qquad (3.28)$$

The above expression can be written in as a function of the angle θ, which results in:

$$q_\theta = -\frac{V_z}{I_{yy}} \int_0^\theta t \cos\theta \, r d\theta \qquad (3.29)$$

$$q_\theta = -\frac{V_z}{I_{yy}} t_{sk} R^2 \sin\theta_i \qquad for \quad 0 < \theta_i < 2\pi \qquad (3.30)$$

Equation 3.30 shows that the shear flow has a sinusoidal shape with maximum values at the neutral line as expected. Finally, the shear force acting on each node can be computed by integrating the calculated shear flow over the respective skin element, resulting in:

$$Q_i = -\frac{V_z}{I_{yy}} \bar{t} R^2 \sin\theta_i R(\theta_{i+1} - \theta_i) \qquad (3.31)$$

3.4.5. BOUNDARY CONDITIONS

The general finite element problem is defined according to:

$$\{F\} = [K]\{U\} \qquad (3.32)$$

Where $\{F\}$ is the system of nodal loads applied to the model, $[K]$ is the stiffness matrix of the structure and $\{U\}$ is the system of nodal displacements. The former can be obtained with the methods described in the previous subsection and the stiffness matrix can be constructed by a process of combining the individual matrices of each element, depending on how they are connected.

However, before restrictions are applied to the model, the determinant of the global stiffness matrix is zero, meaning there are no solutions to the system or there are infinite solutions. In order to have a determinate and unique solution, boundary conditions are required to constrain the model. It is clear that the boundary conditions must be representative of how the model is restrained in reality to obtain a solution with physical meaning.

The standard procedure when studying fuselage sections is to simulate the interaction of the tank with the remaining fuselage by constraining the nodes along one of the main frames, while all other nodes are kept free. Particularly relevant to hydrogen tanks, this approach was used by Gomez et al for the structural analysis in his research [14]. However, this approach increases the local stiffness of the model near the restraint nodes, leading to unrealistic stress concentrations. As a result, the structure may be oversized and heavier than required.

One solution to this problem is to utilize the inertia relief option in NASTRAN, which is commonly employed in the aerospace industry to analyze objects in flight. This option uses the structure's inertia to create a state of static equilibrium, allowing the model to be solved. In practice, NASTRAN applies accelerations to the structure to balance the accelerations caused by the applied loads. In this manner, it is possible to avoid the unrealistic stress concentrations caused by typical boundary conditions. Reference [50] provides extensive examples for the use of inertia relief method in the modelling of different structures in NASTRAN. In chapter 4, a comparison is performed between both strategies of constraining the model confirming the superior performance of the option with inertia relief.

3.5. SIZING APPROACH

In this section, the mathematical formulation of the optimization problem is defined. First, the objective of the optimization is defined, followed by a selection of the design variables. Finally, the design constraints that the optimizer must respect are formulated.

3.5.1. OBJECTIVE

The mass minimization of the external shell structure is selected as the objective function of the optimization and is the sum of the mass of the skin, stringers and frames, as defined in equation 3.33. Each mass is calculated within NASTRAN from the component volume and the material density defined in the model. The optimization is considered converged when the difference between design cycles is below 5 kg, as this value showed the best compromise between accuracy and computational cost.

$$m_{wall_o} = m_{sk} + m_{str} + m_{fr} \tag{3.33}$$

3.5.2. DESIGN VARIABLES

As this work concerns a sizing optimization, the parameters that define the shape and topology of the structural model are fixed for each optimization, including the tank length, radius and number of stiffeners. Based on this layout, geometric design variables are selected to have control over the size of the individual components. The variables allowed to change are the thickness of the tank skin and the dimensions of the stiffening elements. More specifically, the thickness and height of the stringers and the thickness of the frames. Note that the frame height impacts both the radius and length of the tank and therefore is fixed for the analysis.

Table 3.4 summarizes the selected design variables, including their minimum and maximum allowed values, which define the boundaries of the design space. The lower bounds are based on manufacturing limits, while the upper bounds ensure a wide design space without producing unrealistic designs. As all design variables describe dimensional parameters and all use the same unit, a unique step size of 0.1 mm was applied, limited by manufacturing tolerances. To allow more flexibility to the optimizer, the thickness of the tank domes was defined as a design variable, independent from the cylindrical section of the tank. Going one step further, the tank cross section is divided into two

regions, as depicted in figure 3.14, allowing the skin panels and the stringers on the top and bottom to have different dimensions than the sides of the tank.

Description	Lower bound	Upper Bound	Unit
Skin thickness top/bottom (t_{sk1})	0.5	15	mm
Skin thickness sides (t_{sk1})	0.5	15	mm
Dome Thickness (t_{skd})	0.5	15	mm
Stringer Thickness top/bottom (t_{str1})	0.5	10	mm
Stringer Thickness sides (t_{str2})	0.5	10	mm
Stringer Height top/bottom (h_{str1})	20	120	mm
Stringer Height sides (h_{str2})	20	120	mm
Frame Thickness (t_{fr})	0.5	15	mm

Table 3.4: Definition of the design variables and design space
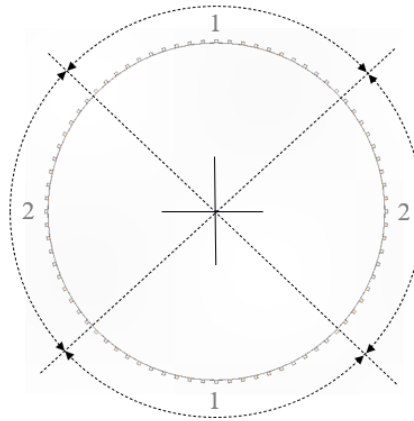
Figure 3.14: Division of the cross section in two distinct regions

3.5.3. DESIGN CONSTRAINTS

The optimization is subject to design constraints, which drive the optimizer to structural solutions that do not fail under the applied loads. While various failure modes exist, three categories are usually selected in the preliminary sizing of aircraft structures: material yielding, buckling instability and fatigue failure. Table 3.5 gives a summary of the constraints and the respective elements covered. The mathematical formulation behind each failure mode is explained in the subsections that follow. Whenever applicable, a safety factor (SF) of 1.5 is applied.

YIELDING

The yielding criteria aims to prevent permanent deformation in the structure under the limit loads, as required by CS-25 guidelines [35]. It is directly related to the strength of the structure and is imposed by comparing the stress in each element against the material yield stress (σ_y), resulting in constraints for the skin panels and stiffeners:

$$R_{yield} = \frac{\sigma}{SF.\sigma_y} < 1 \tag{3.34}$$

Where σ is the stress measured on the finite element model. In particular, the von Mises stresses are used for the skin panels and the maximum stresses are retrieved for each stiffener element.

Constraint	Region
Strength	Skin (top, bottom, sides and domes)
	Stringers (top, bottom and sides)
	Frames
Skin buckling	Skin (top, bottom and sides)
Column buckling	Stringers (top, bottom and sides)
Fatigue	Skin (top, bottom, sides and domes)
	Stringers (top, bottom and sides)
	Frames

Table 3.5: Summary of constraints and regions of application

BUCKLING

Buckling is an important failure mode to consider when the structure is under compression loads. This is specially important in aircraft structures consisting of thin plates, supported by slender stiffeners. In order to prevent this phenomena, the critical stresses at which the structure becomes unstable must be determined.

First, the stability of the skin panels between stiffeners is ensured by limiting the combined compressive and shear stresses on the panels according to equation 3.35. Note that no safety factor is used here as this condition is expected to occur at limit loads.

$$R_{sk_b} = \frac{\sigma}{\sigma_{b_{sk}}} + \frac{\tau}{\tau_{b_{sk}}} < 1 \tag{3.35}$$

Figure 3.15: Stiffened panel geometry
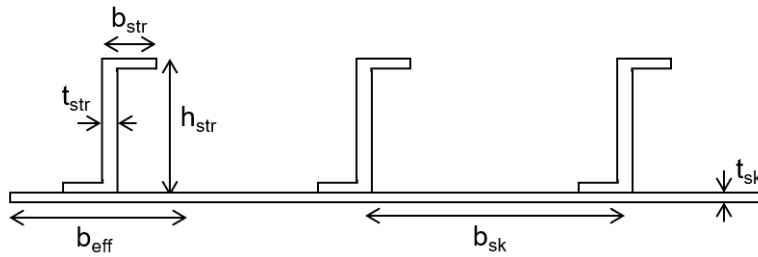
Following the geometry of figure 3.15, the critical buckling stresses are calculated following simple shell buckling formulas, considering the distance between stringers as the panel width.

$$\sigma_{b_{sk}} = K_\sigma \frac{\pi^2.E}{12(1-\nu^2)} (\frac{t_{sk}}{b_{sk}})^2 \tag{3.36}$$

$$\tau_{b_{sk}} = K_\tau \frac{\pi^2.E}{12(1-\nu^2)} (\frac{t_{sk}}{b_{sk}})^2 \tag{3.37}$$

From equations 3.36 and 3.37, it is evident that reducing the space between stringers increases the critical buckling stresses, improving the panel stability. As the expressions depend on the skin thickness t_{sk}, which is a design variable, they must be updated at every iteration to reflect the changes in the model. In NASTRAN, this can be implemented with the use of DEQATN entries. The factors K_σ and K_τ are buckling coefficients which depend on the panel dimensions and the edge supports. As the stiffeners are thin wall members with poor resistance to rotation, it is reasonable to assume that the skin panel is simply supported on all sides. Knowing the panel dimensions, the coefficients can then be estimated using the plots in figure 3.16 (where a/b = frame pitch/stringer pitch). As skin panels are usually narrow with a/b > 3, K_σ can be assumed equal to 4 and K_τ equal to 5.35, as done in [38].

(a) Compressive buckling coefficient

(b) Shear buckling coefficient
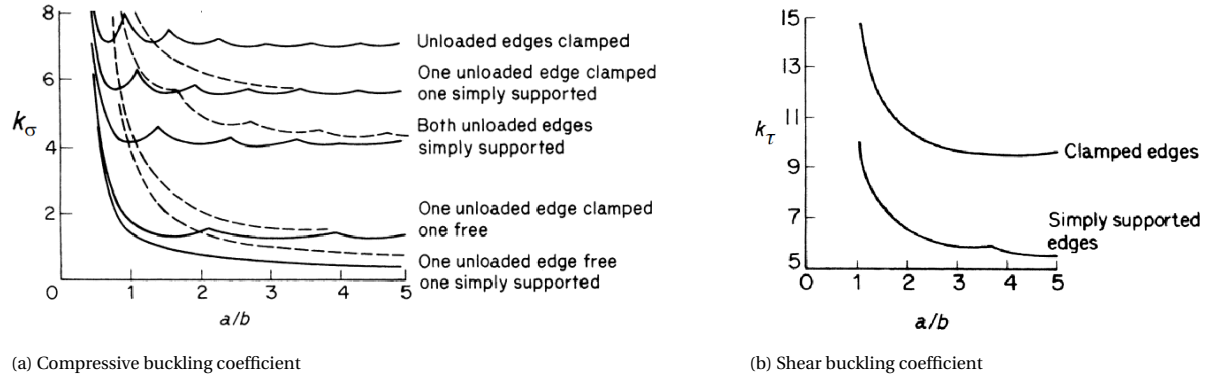
Figure 3.16: Buckling coefficients for flat plates in compression, retrieved from [45]

STRINGER COLUMN BUCKLING

After a certain stress level, the skin starts to buckle and only skin sections close to the stringers remain effective at carrying additional load. At this condition, the stringers can buckle as columns, with their length determined by the distance between frames. Similarly to the previous criteria, the stringer is assumed to be simply supported by the frames, with both ends free to rotate. The constraint function for stringer column buckling is defined in equation 3.38.

$$R_{str_b} = \frac{\sigma}{SF.\sigma_{b_{sk}}} < 1 \tag{3.38}$$

The critical load and stress at which the stringer will buckle are calculated according to formulas by Euler, given in equations 3.39 and 3.39, respectively. Again, DEQATN entries are used to apply this constraint during the optimization.

$$P_{Euler} = \frac{\pi.E.I}{L_{fr}^2} \tag{3.39}$$

$$\sigma_{b_{sk}} = \frac{\pi.E.I_{xx}}{L_{fr}^2.A} \tag{3.40}$$

FATIGUE

Finally, a constraint on fatigue is imposed to prevent structural failure under cyclic loads. When the structure is subject to repetitive loads, small cracks may form and propagate, leading to failure. The stress values at which these cracks appear are usually significantly lower than the material yield strength.

$$R_{Fat} = \frac{\sigma}{SF.\sigma_{Fat}} < 1 \tag{3.41}$$

Here, σ_{Fat} is calculated using the general fatigue life model, from Rubiae [49]. The fatigue behaviour of the material is predicted by:

$$\log N = A - B \log(k_t^E \sigma (2 - \frac{2\sigma_m}{\sigma})^C - D) \tag{3.42}$$

Where N is the number of cycles to failure, and σ_m and σ are the mean and maximum applied stresses. The factors A to E depend on the material characteristics and were retrieved from the study by Rubiae [49]. K_t is a stress concentration factor introduced to account for geometric discontinuities in the structure, such as holes or keyways, which can lead to crack initiation or propagation. A factor of 4.5 was assumed with a sensitivity study performed in chapter 5.

In order to relate the mean to the applied stress, the exceedance frequency model proposed by NLR is used [51]. In this model, the stress levels at 1g flight are taken as reference and scaling factors are empirically determined for each exceedance frequency, considering 40000 flights of 1.5h. As an example, the scaling factor for 100 exceedances is 2.215, meaning that 100 times per 60000 flight hours, the stress on the structure exceeds the "steady flight" stress by a factor of 2.215. As 60000 flight hours matches Airbus' Design Service Goal (DSG) for the A320 family, which is the value used for design and validation of the maintenance programme [52], this model is suitable to be used in this research. Using the relation in equation 3.43 and $\sigma_m = \sigma_{1g}$, the stress value can be calculated according to equation 3.44.

$$\sigma = scale.\sigma_m \tag{3.43}$$

$$\sigma = \frac{(N * 10^{-A})^{-\frac{1}{B}} + D}{(k_t^E (2 - \frac{2}{Scale})^C} \tag{3.44}$$

In a conservative approach, the stress was calculated for each exceedance frequency in table 3.6 and the minimum was taken for the fatigue constraint.

Exceedance frequency	Scale
10^1	2.6
10^2	2.215
10^3	1.916
10^4	1.628
10^5	1.419
10^6	1.247

Table 3.6: Standardized load spectrum for 40000 flights [51]

3.6. DESIGN OF EXPERIMENTS (DOE)

In order to identify the most efficient tank topology, a DOE was performed changing the frame height, number of frames and number of stringers between designs. The frame height impacts not only the tank radius but also the tank length, since all designs are required to carry the same hydrogen fuel mass.

In a similar way to the design variables, the bounds of design space for the DOE were set wide enough, without running the risk of producing unrealistic tank designs. The frame height ranged from the maximum allowed stringer height in the optimization to the reference frame height found in an A320 multiplied by a factor of safety. This is because higher frames may be required to comply with crash tests. The maximum number of stringers was limited by the perimeter of the tank, ensuring a stringer spacing of at least the stinger width. The minimum number was set to 20 to have a wide design space. The number of frames covered frame pitch range studied in [38] and should therefore capture the optimum design. Table 3.7 summarizes the values selected.

Design Variable	Lower bound	Upper bound	Unit
Frame height (h_{fr})	20	200	mm
Number of frames (n_{fr})	6	28	-
Number of Stringers (n_{str})	20	80	-

Table 3.7: Definition of the design variables and design space for DOE

Note that designs with high number of frames and low number of stringers can create skin panels with low ratio of frame pitch to stringer pitch. As a result, higher buckling coefficients should be used, which, in turn, would increase the critical buckling stresses. By maintaining the values of k_σ and k_τ constant for every design, some accuracy is lost but a conservative approach is followed.

Within the designed space defined, 40 cases were retrieved following a latin hypercube sampling method. Figure 3.17 shows the distribution of the experiment points within the design space.
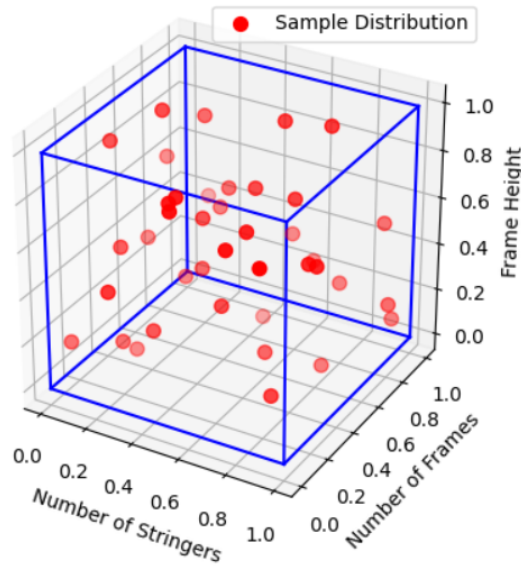
Figure 3.17: Sample distribution of DOE

4

VERIFICATION

Before extracting the results, it is crucial to assess the validity and accuracy of the framework proposed in this research. This is a fundamental step to ensure the results can be trusted and used in a future analysis. The following sections evaluate several different aspects of the method, including the quality of the finite element model, the load application strategy, the mesh size and the optimization routine.

4.1. RIGID BODY MODES

First, the finite element model is checked for the presence of rigid body modes, in an unrestrained solution. Six rigid body modes were found corresponding to the free translations and rotations in the six directions of motion, confirming that the model is not artificially restrained. Additionally, the first flexible mode was verified to ensure it represented a realistic response of the structure, with the results depicted in figure 4.1. With this check completed, there is confidence that there are no errors in the generation of the finite element model.
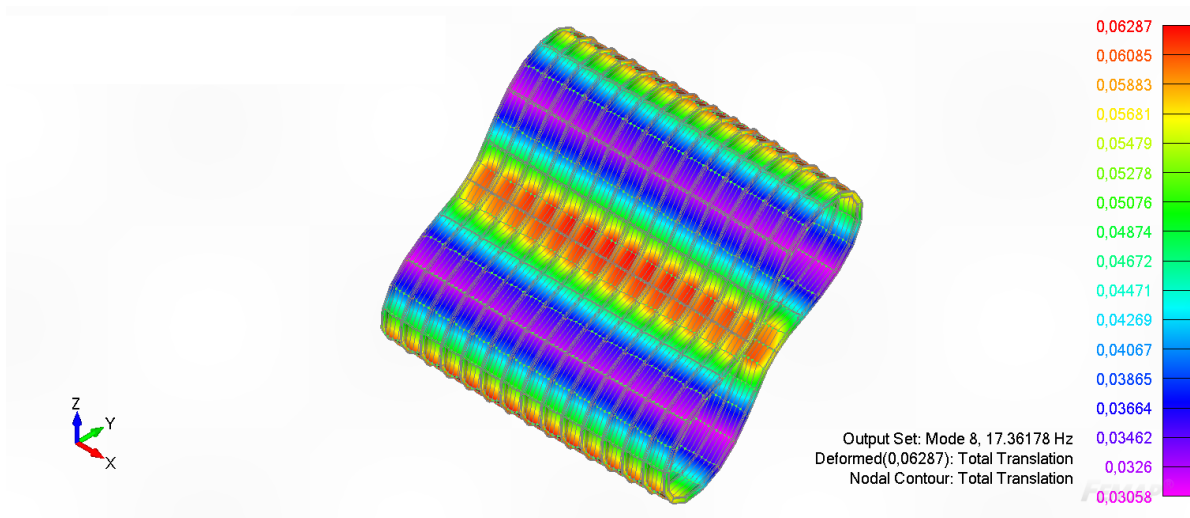
Figure 4.1: Seventh normal mode (first flexible mode) of the baseline structure, without domes

4.2. LOAD APPLICATION

The structural response of the model to the selected loads is dependent on how the loads are applied. Therefore, it is critical to verify not only that the equivalent loads produce the correct bending moment and shear force but also that the structure responds in the expected manner. To this end, an aluminium test cylinder stiffened with C-frames and Z-stringers was used, with dimensions and loads adapted from a structural fuselage study and summarized in table 4.1. Note that the pressure was changed to negative to reflect the external pressure acting on the tank wall.

Parameter	Value	Units
Tank length (L)	970	mm
Tank radius (R)	250	mm
Skin thickness (t_{sk})	1.0	mm
Stringer thickness (t_{str})	1.0	mm
Stringer height (h_{str})	20	mm
Stringer width (b_{str})	15	mm
Frame thickness (t_{fr})	1.2	mm
Frame height (h_{fr})	40	mm
Frame width (b_{fr})	20	mm
Pressure (P)	55000	Pa
Bending moment (M)	4000	Nm
Shear Force (Q)	600	N

Table 4.1: Dimensions and loads of the aluminum test tank, adapted from [38]

Figure 4.2 shows that the equivalent nodal loads generate the desired bending moment and shear force, with errors in the order of 1e-6, regardless of the number of stringers.
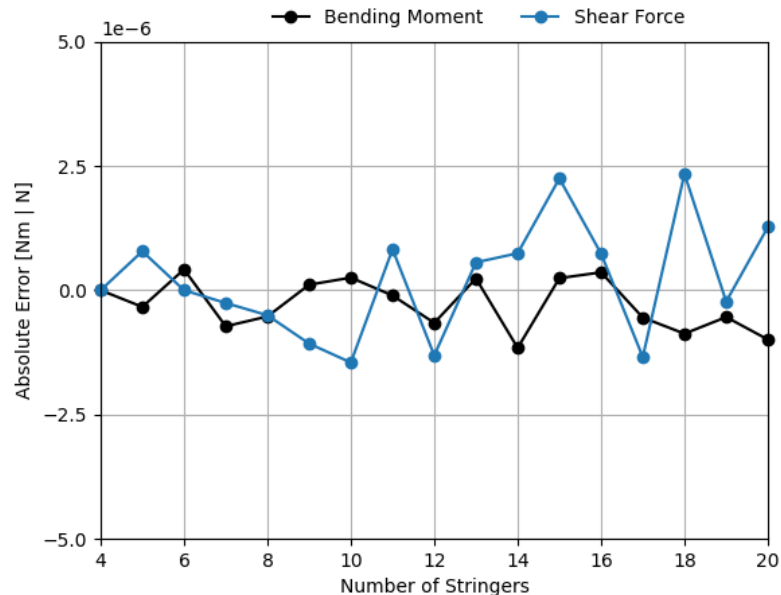
Figure 4.2: Load application validation

Figure 4.3 displays the minor principle stresses on the skin when only external pressure is applied. It is noteworthy that the skin panels between the stiffening elements are under compression and

therefore susceptible to failure due to buckling. It can also be seen how the stringers and frames alleviate the compressive stresses on the skin, which is in line with the mathematical relations defined earlier in this research. Finally, the domes appear to have a good resistance to the external pressure, even though they are not stiffened.
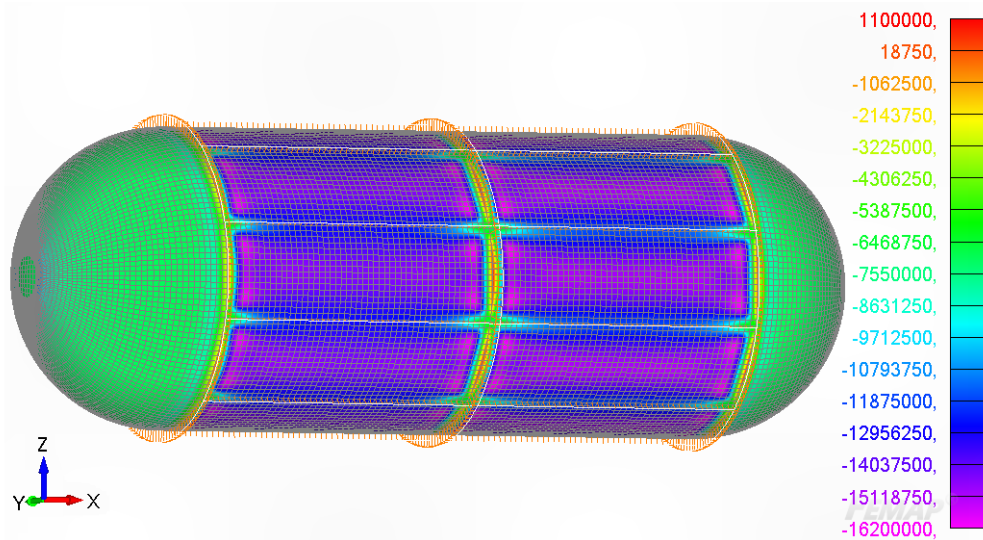
Figure 4.3: Mean stresses on the tan skin under an external pressure load

Figure 4.4 shows the longitudinal stresses on the skin under a positive bending moment about the 'Y' axis. As expected, the highest stresses are found on the top and bottom. panels with the former being under compression and the latter under tension. On the contrary, the stresses on the side panels are low, since they are close to the neutral line of the structure. The same observation can be made for the stiffeners, as depicted in figure 4.5. For the same reasons, moments about the 'X' axis due to lateral load cases put the side panels under tension and compression, with minimal impact on the top and bottom panels.
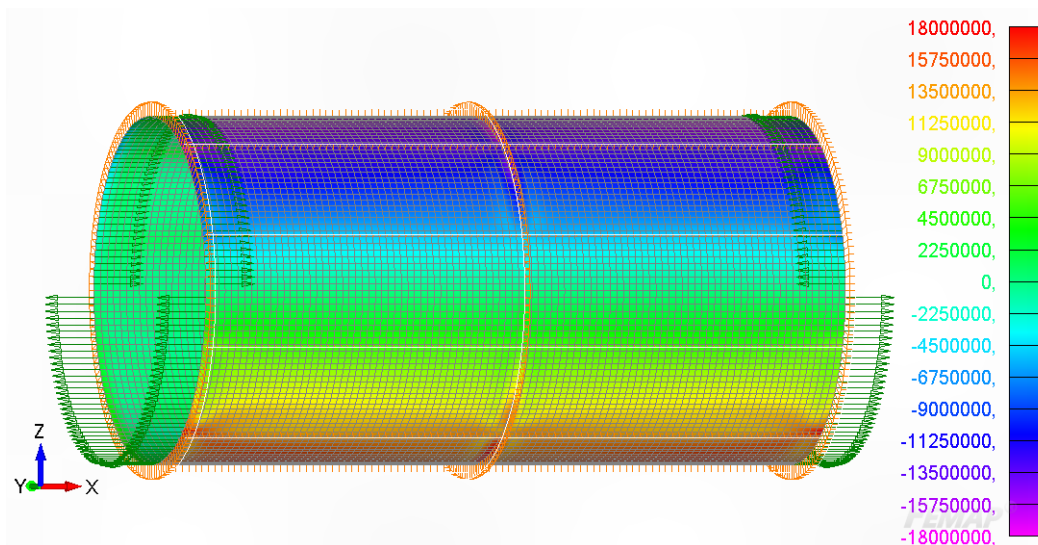
Figure 4.4: Longitudinal stresses on the skin under a positive bending moment
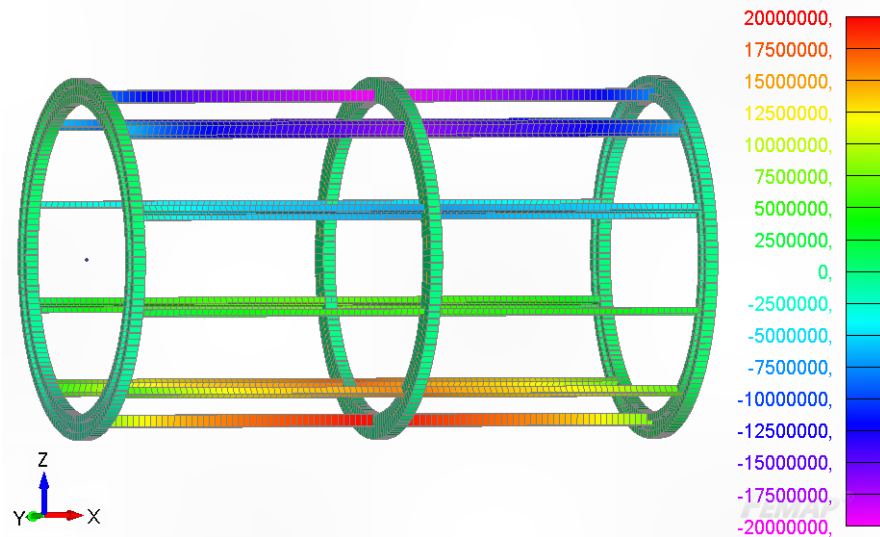
Figure 4.5: Stresses on the stiffeners under a positive bending moment

The structural response under shear loads was also evaluated. Figure 4.6 shows the distribution of shear stresses on the skin under a positive shear load in the vertical direction. As anticipated, the shear stresses are coherent with the shear flow on the section, which takes on a sinusoidal shape.
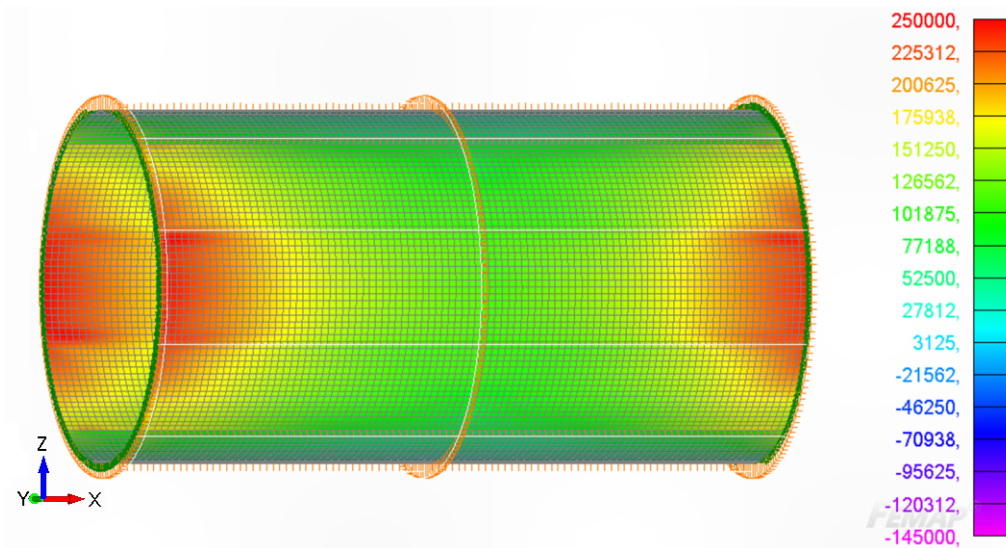
Figure 4.6: Shear stress on the skin under a positive shear force

4.3. MESH CONVERGENCE

A mesh convergence study was performed to evaluate the impact of mesh density on the results. To accomplish this, the sizing procedure was repeated for different mesh refinements by increasing the number of elements between stringers up to the limit allowed by the computational power available. Figure 4.8 displays the coarsest and finest meshes considered in the study, with 1 and 10 elements between stringers, respectively.
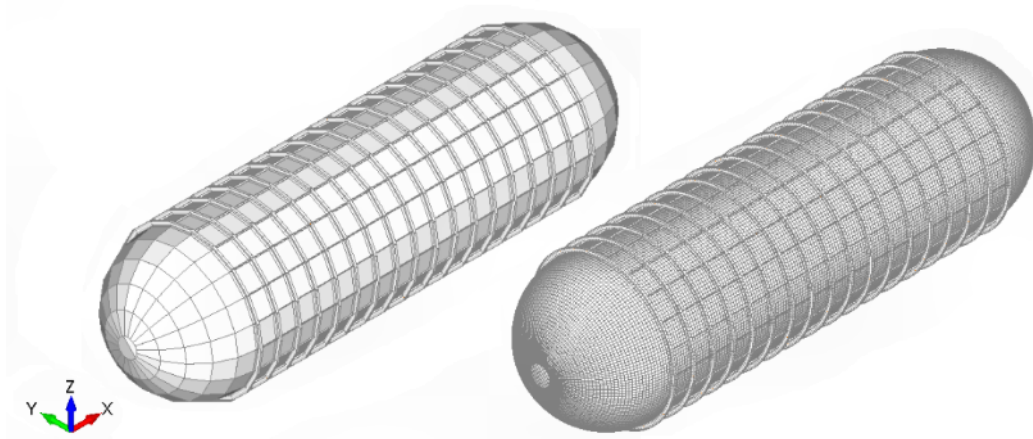
Figure 4.7: Coarsest and finest meshes with a total number of elements of 3360 and 295200, respectively

The results obtained are depicted in figure 4.7, comparing the solver time with the accuracy of the response, expressed as the absolute error relative to the mass obtained with the finest mesh. As expected, refining the mesh improves the accuracy, at the cost of a higher computational time. However, after a certain number of elements, the solver time increases significantly more than the error, indicating that the results are sufficiently converged. Based on these results, a mesh with 8 elements between stringers was chosen for the analyses in this research. When compared to the solution obtained with 10 elements between stringers, it is 6.75% faster, while converging to a mass just 0.04% lower. This choice ensures that the optimization outcomes are not significantly influenced by the mesh density.
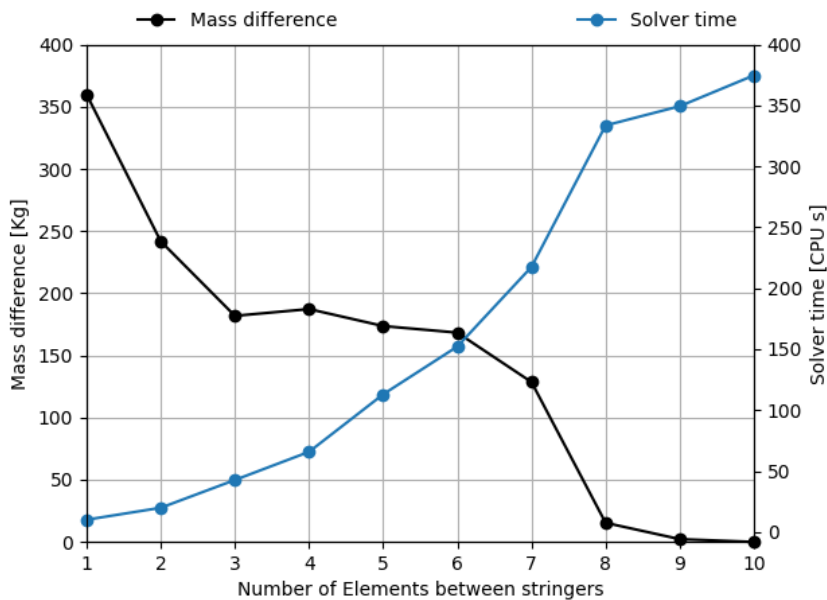
Figure 4.8: Mesh convergence plot

4.4. PRESSURE VESSEL CASE

Finally, the optimizer routine is tested by using a benchmark case with a known analytical solution. The case selected involved a cylindrical shell with a radius of 0.5 m and a length of 2 m, that was subjected to an internal pressure of 100 kPa. The objective was to minimize the structural mass of the shell by optimizing the skin thickness, while limiting the hoop stresses on the skin to 85 MPa. Starting from a value of 1 mm, equation 3.1 gives an exact solution of 0.59 mm, if no factor of safety is considered.

Two cases were analyzed. In the first case, the inertia relief option was used to constrain the model and converged to a skin thickness of 0.59 mm, matching the analytical solution. In the second case, the nodes at one end of the shell were fixed in all degrees of freedom, following the approach of Gomez [14]. However, this resulted in a skin thickness of 0.62 mm, exceeding the exact value by 5.1%. Figure 4.9 shows the distribution of hoop stresses on the models, revealing the unrealistic stress concentration near the boundary condition that led to the error in the results. The comparison between these two strategies shows that the inertia relief option in NASTRAN is the appropriate choice for this application, minimizing the errors caused by boundary conditions.

(a) Inertia Relief   (b) AFT end fixed
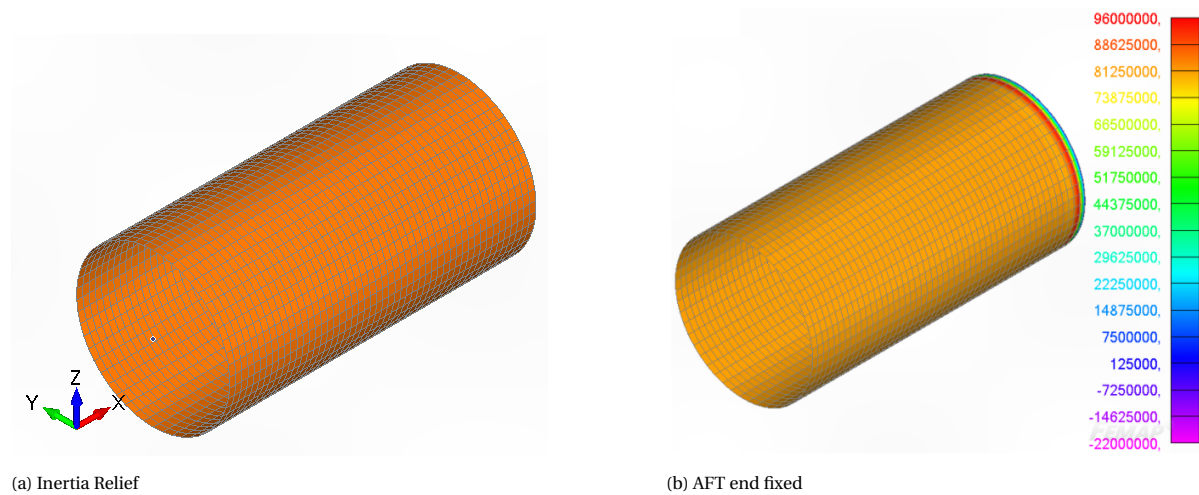
Figure 4.9: Contour of circumferential (hoop) stresses on the FE model

5

ANALYSIS AND RESULTS

The method described in this research was used to size the structure of an AFT tank integrated into an A320-200. In particular, the hydrogen versions generated by Onorato were used, as they already reflect the required changes at aircraft level to integrate the hydrogen tank(s) and therefore provide a realistic sizing scenario [16].

This chapter presents and discusses the results of the work. First, the loads acting on the fuselage of each aircraft are determined, based on the mass distribution. Right after, the results of the DOE are described, giving insights about the most suitable tank topology. Then, both the impact of the stringer shape and dome shape are assessed, followed by a sensitivity analysis on specific fixed input variables. Finally, the chapter closes with a comparison of the results obtained with those presented by Onorato for the same configurations and top-level requirements.

5.1. AIRCRAFT CONFIGURATIONS AND LOADS

Three aircraft geometric models were built based on available data. First, a baseline model recreates the reference aircraft, following data from Airbus. The variant used is the WV0055 with a MTOM of 79.0, a OEM of 45.0t and 150 passengers distributed over two classes [53]. Then, two hydrogen variants are built based on data from Onorato. The first has a single AFT tank behind the passenger cabin, while the second has both an AFT and a FWD tank. Both AFT tanks have an integral structure, while the FWD tank is non-integral. These variants correspond to aircraft SMR-LH2-b and SMR-LH2-e in Onorato's research. Although it would have been possible to model the hydrogen aircraft directly, the baseline aircraft serves two purposes. First, it allows a validation of the mass estimation methods against reference data from Airbus. Second, it provides a baseline to gain insights on how integrating the tanks changes the distribution of loads across the fuselage. The properties of the 3 aircraft are summarized in Table 5.1.

Table 5.1 demonstrates a strong match between the baseline model and the reference aircraft data, confirming the accuracy of the mass estimations. Regarding the hydrogen variants, it is interesting to see that while the OEM increases due to the fuselage extension and the addition of the hydrogen tanks, MTOM actually decreases due to the lower fuel mass of hydrogen fuel compared to kerosene, which is in line with the conclusions from Onorato and Silberhorn [9, 16].

Parameter	Reference	Baseline	Aft	Fwd & Aft	Unit
OEM	45.0	45.1	51.4	51.3	t
PM	19.3	19.3	19.4	19.3	t
MZFM	64.3	64.4	70.8	70.7	t
FM	14.7	14.7	5.7	5.6	t
MTOM	79.0	79.1	76.5	76.2	t
Fuselage Length	37.57	37.57	45.10	48.26	m

Table 5.1: Properties of baseline aircraft and hydrogen variants

Based on the aircraft models, internal fuselage loads in the form of shear force and bending moment were determined for each of the load cases defined in section 3.3. Figure 5.1 highlights the maximum values obtained, corresponding to symmetric manoeuvres with a load factor of 2.5g and side-slipping flights in an engine out condition. The loads computed for the remaining cases can be seen in appendix A. The graphs clearly indicate that the fuselage of the hydrogen aircraft is subject to higher loads, particularly at the wing position, as the wing loses the bending relief from the kerosene fuel. Moreover, there is an increase in bending moment and shear force as the length of the fuselage increases.

(a) Shear Force due to 2.5g pull-up

(b) Bending Moment due to 2.5g pull-up

(c) Shear force due to engine-out

(d) Bending Moment due to engine-out
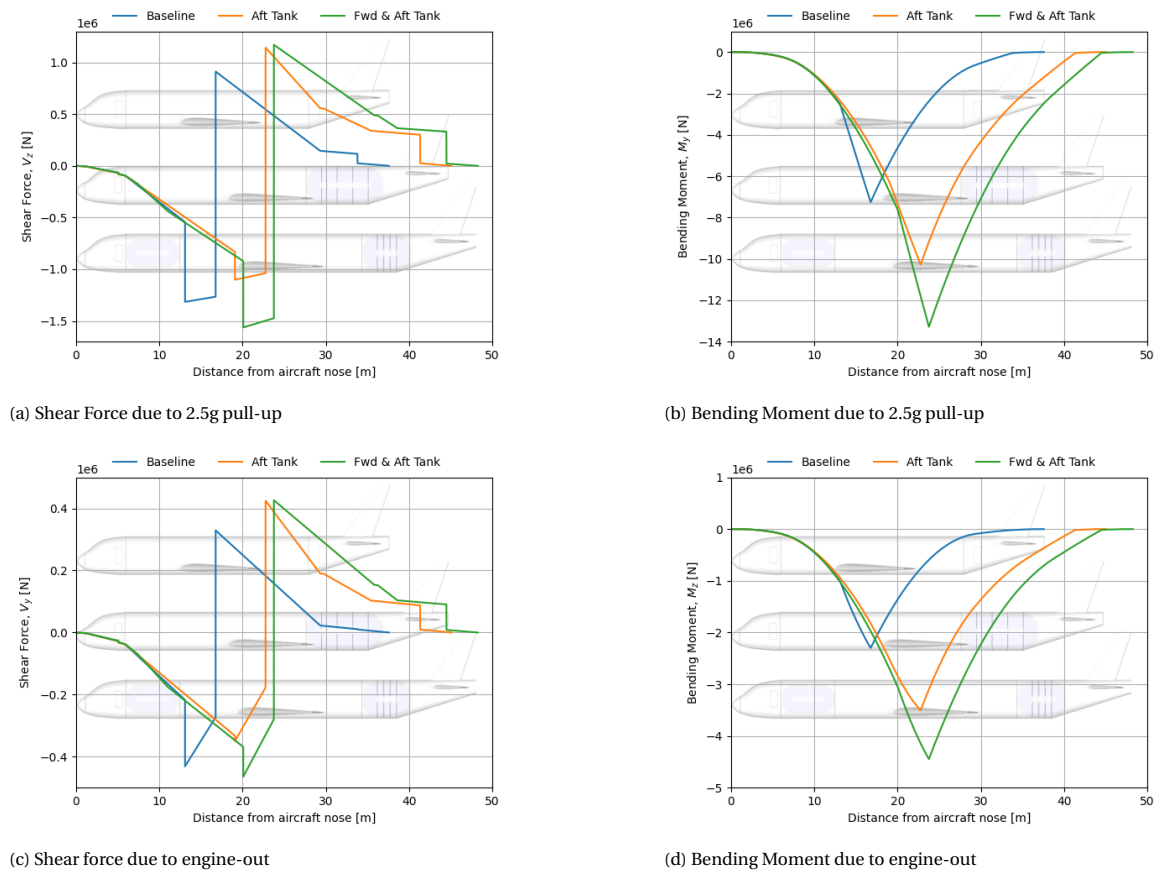
Figure 5.1: Shear force and bending moment diagrams for the baseline aircraft and hydrogen variants

The loads required for the sizing of the tank structure are retrieved at the location of the first tank frame and are summarized in table 5.2.

Load	Case		Unit
	AFT	AFT & FWD	
External Pressure P	-21.66	-21.66	KPa
1g			
Shear Force V_z	168.23	200.75	KN
Bending Moment M_y	-1792.26	-1250.31	KN.m
2.5g			
Shear Force V_z	415.92	495.74	KN
Bending Moment M_y	-4426.83	-3076.46	KN.m
Engine Out			
Shear Force V_y	133.80	155.89	KN
Bending Moment M_z	-1393.20	-890.33	KN.m

Table 5.2: Structural Sizing loads at the AFT tank

5.2. DOE RESULTS

With the critical sizing loads determined, a DOE was conducted to identify the most efficient tank topology. The frame height, number of frames and number of stringers were changed between designs. As the hydrogen fuel mass was set as a requirement, the tank must be longer in designs with a higher frame height to accommodate the required fuel. Therefore, it is more appropriate to express the results in terms of tank length, frame pitch and stringer pitch allowing a fair comparison between cases and a clear identification of the design trends.

Figure 5.2 summarizes the results obtained, with the full data presented in appendix B. It is clearly noticeable that the best designs utilize the minimum tank length, along with the minimum frame and stringer pitch. The results are consistent with the expectations and follow from the design constraints defined in earlier in the report. The buckling stability of the skin panels is directly related to the stringer pitch. As the stringer pitch reduces, lower skin thicknesses can be used, as shown in figure 5.3a. Similarly, the frame pitch affects the buckling stability of the stringers. Figure 5.3b illustrates that an increase in frame pitch results in an increase in stringer height.
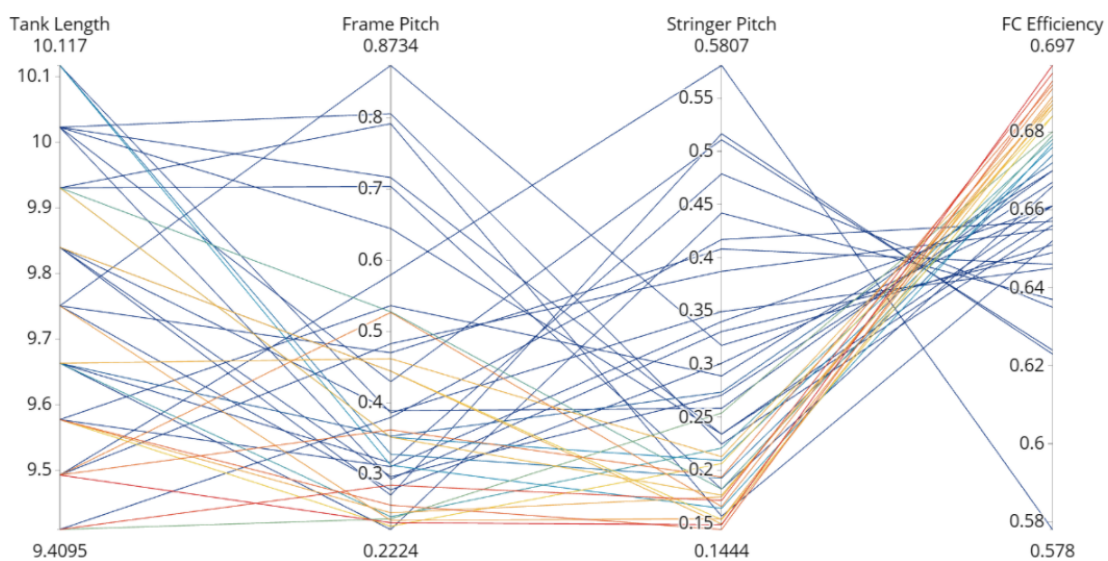
Figure 5.2: Overall results of DOE
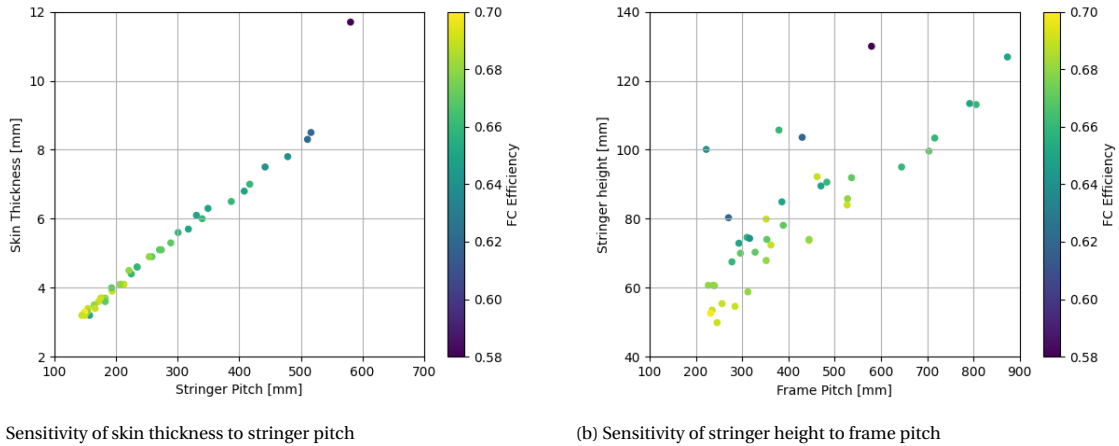
(a) Sensitivity of skin thickness to stringer pitch

(b) Sensitivity of stringer height to frame pitch

Figure 5.3: Sensitivity to changes in stringer and frame pitch

However, it is also interesting to see that higher frame and stringer pitches could be used with limited impact on FC efficiency. To illustrate this, figure 5.4 shows that a FC efficiency of 70% is obtained for a frame pitch of 250mm and a stringer pitch of 150mm. Doubling both the frame pitch to 500mm and the stringer pitch to 300mm results in only a 4% decrease in FC efficiency. Note that the mass of the attachments was included in the allowance of 8% used to estimate the total tank mass. However, using a value proportional to the number of stiffeners would be more realistic, and would likely lead to an optimum design with fewer stiffeners.
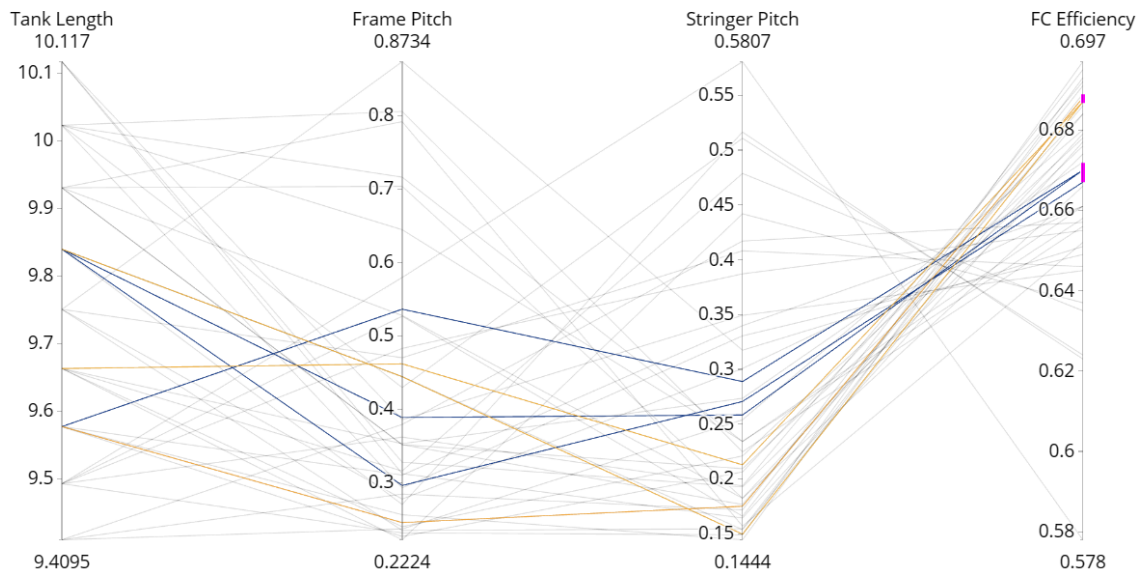
Figure 5.4: Highlighted results of DOE

Based on the results obtained, an optimum combination of the studied variable was selected for the remaining analysis, consisting of 15 frames, 80 stringers and a frame height of 120mm.

To fully understand the process within the optimizer, it is important to track the evolution of the objective function and the design variables during the optimization. Figure 5.5 depicts this variation for the experiment with the highest FC experience. The first observation is that the stiffened wall mass increases during the optimization, as the initial structure fails under the defined design constraints.

At the end of the optimization, the mass of the stiffened wall is more than twice the original mass. This underlines the importance of using a detailed method to size the structure.
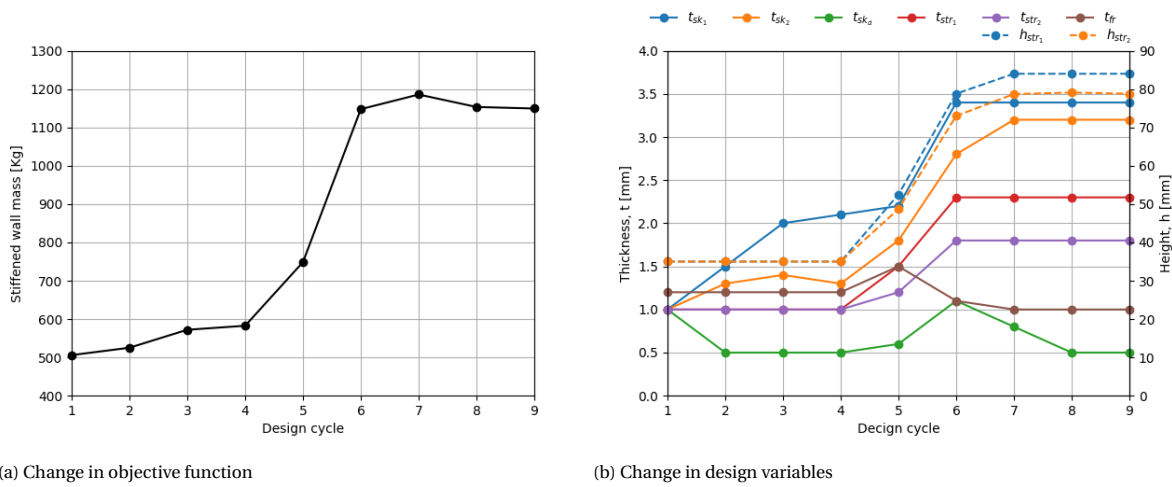
(a) Change in objective function   (b) Change in design variables

Figure 5.5: Change in objective function and design variables

To strengthen the structure, all design variables are increased, with the exception of the frame thickness and the skin thickness in the domes. A closer inspection of the results showed that the frame thickness is not well captured by the design constraints imposed, and consequently, the optimizer decreases its value until reaching the lower bound. The impact of this effect was minimized by increasing the lower bound of this design variable from 0.5 mm to 1.0 mm, which is already taken into account in the results presented.

5.3. STRINGER AND DOME SHAPE

With the main topology of the tank structure defined, more detailed studies can be carried. The geometry of the stiffeners was analysed first, as it influences the behaviour of the shell structure under compression. Typically, HAT-stringers improve the stability of the skin, as they are supported on both sides reducing the unsupported width of the skin. To evaluate if this translates into a mass reduction, a configuration with HAT-stringers was tested and the results were compared to the previous ones obtained with Z-stringers. The results, shown in table 5.3, show that the configuration with HAT-stringers is superior from a gravimetric point of view. It allows lower skin thicknesses, reducing the overall mass of the stiffened wall by 12.9%, and increasing the FC efficiency by 3%. This result provides further confirmation that skin buckling is one of the main criteria driving the design.

Stringer Shape	t_{sk} [mm]	t_{str} [mm]	h_{str} [mm]	m_{wall_o} [kg]	m_{FC} [kg]	η_{FC} [0-1]
Z	3.1	1.8	67.7	1046.7	2467.1	0.70
HAT	2.1	0.6	88.9	727.7	2148.0	0.73

Table 5.3: Comparison between stiffened shells with Z and Hat stringers (average values of design variables shown)

Hence, HAT-stringers were used for the remainder of the study. It should be noted that additional factors would need to be considered to select the best stringer shape for a given application. For instance, if good corrosion resistance is required, Z-stringers may be selected instead of HAT-stingers as the latter tend to trap water within their shape and are more difficult to inspect.

The analysis also took into account the impact of changing the shape of the tank domes. The ratio between the the tank radius and the dome length varied from 1 to 2, with the first corresponding to a spherical dome. It was found that, for the same fuel mass, the external wall mass increases as the dome length decreases, which is explained by the increase in skin thickness to cope with the increasing frame pitch. However, the mass of the internal wall decreases due to the reduction in material. As a result, the change in dome shape does not significantly affect the gravimetric efficiency and other factors must be considered to select the best design. Perhaps the most important parameter is the tank length, which has a direct impact on the fuselage length and passenger capacity. The shortest tank length is obtained with the largest dome factor, theoretically pointing to this option as the most suitable design. In practice, however, it is expected that a transition radius or a knuckle is used to ease the manufacturing, leading to a conservative selection of a dome factor of 1.6 for the research. Also, Brewer found in his study that this was the shape that would result in the lowest operating cost [3].
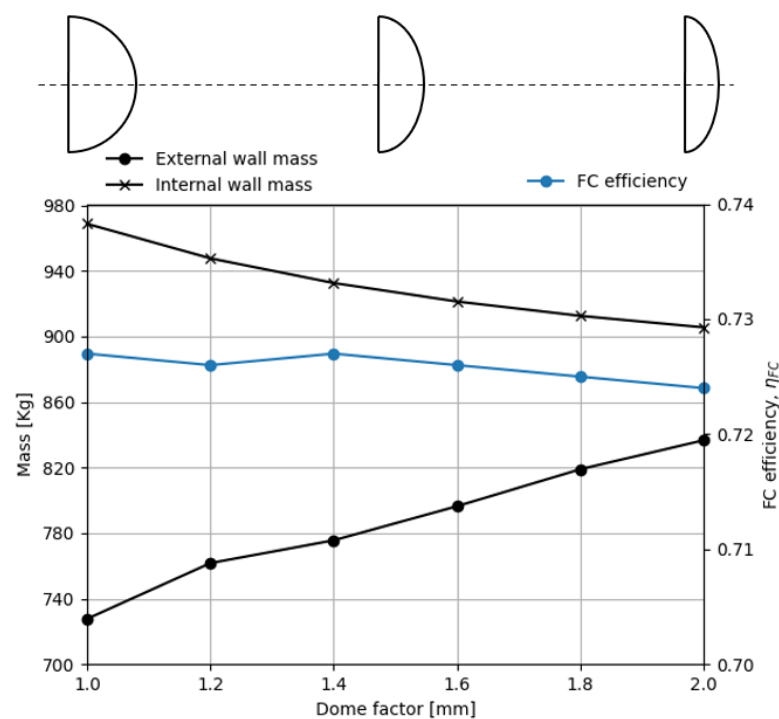
Figure 5.6: Sensitivity to dome factor

5.4. SENSITIVITY ANALYSIS

The results described in the previous sections rely on various input parameters that were defined prior to each optimization. In order to increase the confidence in the results, additional analysis were carried to test the sensitivity of the external wall mass and the tank's FC efficiency to changes in specific parameters.

Figure 5.7 shows the impact of changing the stress concentration factor used in the fatigue constraints. In fatigue design, a stress concentration higher than unity reduces the allowable stress in accordance with equation 3.44. As this research pertains to preliminary design, a conservative value of 4.5 has been employed up to this point. Figure 5.7 shows that, at this value, the fatigue criteria is actively constraining the design. As expected, the mass of the stiffened wall decreases as K_t decreases

and fatigue stops driving the design for values of K_t lower than 2. Given the difficulty in inspecting cryogenic tanks with a double wall construction, it is appropriate to maintain the value of 4.5, providing a higher safety margin for fatigue.
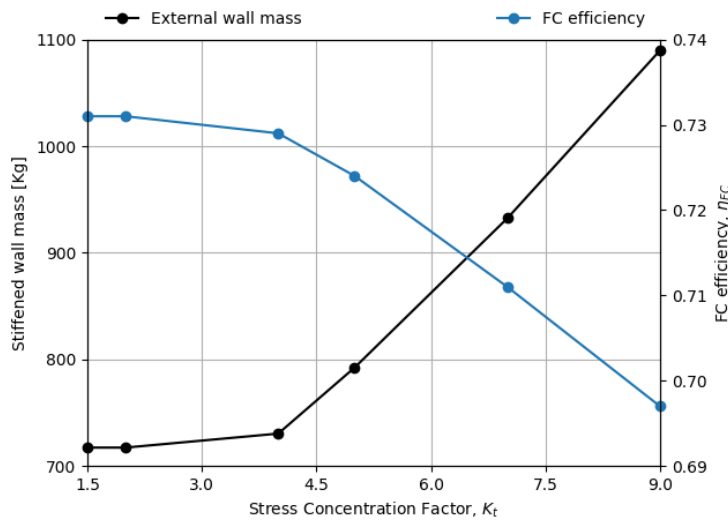
Figure 5.7: Sensitivity to stress concentration factor

Figure 5.8 displays the sensitivity of the results to changes in Maximum Operating Pressure (MOP) and insulation thickness. The pressure studied in this case refers to the internal pressure of the liquid hydrogen, which directly affects the sizing of the inner shell, according to equation 3.1. Increasing MOP increases the thickness of the inner wall and the inner wall mass, lowering the FC efficiency of the tank. Therefore, it is desirable to use the lowest possible MOP, while maintaining a safe value above atmospheric pressure avoiding issues with oxygen ingestion. The impact of MOP on the external shell mass is small and only related to the change in tank length due to the change in the internal wall thickness. The thickness of the MLI insulation was considered constant with respect to MOP, which is a reasonable assumption considering its high thermal performance. The impact on the FC efficiency of varying the insulation thickness is less significant than changes in the MOP, as the density of the insulation material is only 1.6% of the density of inner wall material.
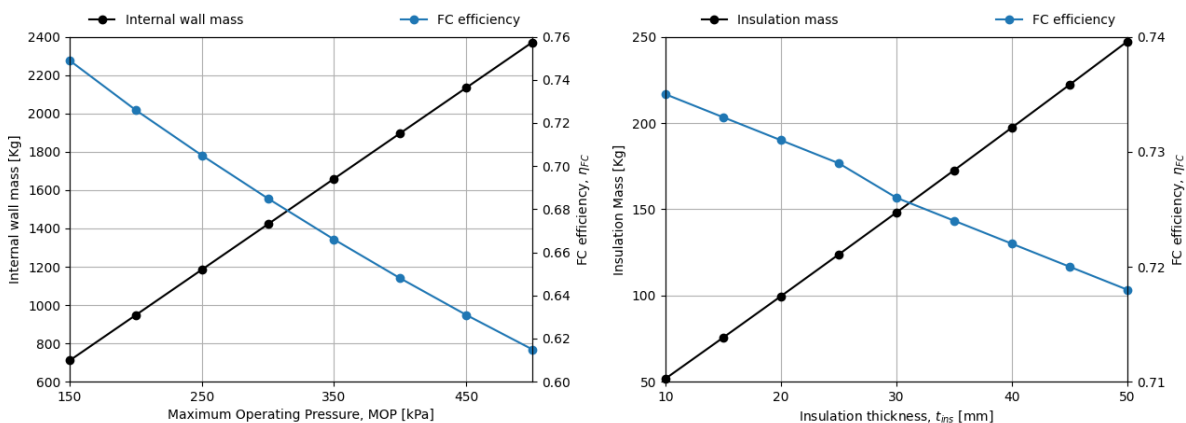
(a) Sensitivity to maximum operating pressure

(b) Sensitivity to insulation thickness

Figure 5.8: Results of sensitivity analysis

5.5. COMPARISON WITH LITERATURE

With the main design trends identified and confidence that the method is working as intended, the results obtained for the AFT tank can be compared to the ones obtained by Onorato, for the same aircraft configuration and top level requirements. The characteristics of the tank design are shown in table 5.4.

Parameter	AFT		FWD&AFT		Unit
	Onorato	New Solution	Onorato	New Solution	
Fuel mass (FM)	5658.9	5658.9	3213.1	3213.1	Kg
Fuselage radius (r_{fus})	1.99	1.99	1.99	1.99	m
Venting Pressure (P_{vent})	250	250	250	250	KPa
Tank length (l_{tank})	8.93	8.43	5.67	5.14	m
Dome ratio (l_{tank})	-	1.6	-	1.6	-
Number of stringers (n_{str})	-	80	-	80	-
Number of Frames (n_{fr})	-	15	-	7	-
Inner shell thickness (t_{wall_i})	2.7	4.0	2.7	4.0	mm
Insulation thickness (t_{ins})	121.5	30.0	136.1	30.0	mm
Outer shell thickness (t_{wall_o})	-	1.3 (avg)	-	1.5 (avg)	mm
Fairing thickness (t_f)	1.6	1.6	1.6	1.6	mm
Inner shell mass (m_{wall_i})	1243.0	1089.2	727.9	661.1	Kg
Insulation mass (m_{ins})	430.4	131.5	308.3	79.9	Kg
Outer shell mass (m_{wall_o})	-	749.2	-	387.0	Kg
Fairing mass (m_f)	96.8	93.1	43.8	42.9	Kg
Divider mass (m_{div})	94.4	94.4	94.4	94.4	Kg
Truss system mass (m_{truss})	255.5	-	157.9	-	Kg
Total tank mass (m_{FC})	2289.6	2329.5	1390.5	1366.0	Kg
FC efficiency (η_{FC})	0.71	0.71	0.70	0.70	-

Table 5.4: Comparison of tank performance with results from Onorato [16]

The first observation is that the thickness of the internal shell is higher in the tanks proposed in this research, for two main reasons. First, both tanks are sized for the same MOP inside the tank, but the pressure difference is higher in the tank with vacuum insulation. Second, in this method, an increased safety factor was used to account for hydrostatic and thermal loads, resulting in a more conservative estimation.

In order to allow a fair comparison of the fuel containment mass and efficiency, some modifications were made to the results retrieved from Onorato. The most striking concerns the mass calculation of the inner shell. In the integral tank concept used by Onorato, the inner vessel is the load bearing structure of the tank and therefore is stiffened with stringers and frames. However, the mass of the stiffeners is not included in the results provided by the author. Hence, the empirical relation from Torenbeek described in section 3.3 was used. The mass of the truss system required to connect the tank to the fuselage airframe was also added. In the work from Brewer, this mass represented approximately 10% of the fuel containment mass and therefore, that value was adopted here[3].

With the above modifications, the FC mass obtained with the new solution was found to be 1.7% higher than that obtained by Onorato in the configuration with a single AFT tank and 1.8% lower

in the configuration with both an AFT and a FWD tank. As a result, for each configuration, the FC efficiency of the new solution matches the data presented by this author. It can also be observed that a higher FC efficiency was achieved with the longer tank. While the difference was only 1 percentage point, it is in line with trends identified by Onorato [16] indicating that higher efficiencies can be expected for larger tanks used in long-range aircraft, for example.

Looking closer at the results in table 5.4, it can be seen that the small mass difference in the results is due to the mass of the foam insulation and the truss system in the existing concept, which negate the advantage of not having an outer shell. As previously discussed in chapter 2, it is likely that a double wall architecture would be required even with foam insulation, decreasing the efficiency of this concept.

6

CONCLUSIONS AND RECOMMENDATIONS

This research proposed a new solution to carry liquid hydrogen in the fuselage of commercial aircraft, consisting of an integral tank with a double wall architecture and vacuum insulation. With this design, the integration with the airframe is simplified while ensuring an efficient thermal insulation. Additionally, a method was developed to to evaluate the feasibility of the proposed solution and answer the research question:

How does the fuel containment efficiency of an integral tank compare to existing concepts, when using vacuum insulation and a stiffened external shell?

The method was based on a parametric framework and followed a FE approach, allowing for accurate mass estimations of the external load bearing wall on various different tank designs. Preliminary analysis of an AFT tank for a short/medium range aircraft indicate that buckling stability plays a crucial role in the sizing of vacuum insulated tanks. As a result, optimum designs use a high number of stringers and frames. For the same reason, HAT-stringers were found to be more efficient than Z-stringers.

A comparison with an existing tank design using the same requirements was then performed, showing that very similar results could be obtained. For a configuration with a single AFT tank, the new concept had a slightly higher FC mass (2329.5 kg compared to 2289.6 kg) resulting in the same FC efficiency (0.71). The configuration with a FWD and an AFT tank showed a slightly lower FC mass for thew concept (1366.0 kg compared to 1390.5 kg), leading again to an identical FC efficiency (0.70).

From a gravimetric perspective, it can then be concluded that the proposed solution does not underperform existing designs. In fact, this concept is expected to outperform existing single-wall designs if a second wall is added to address the issues with foam insulation. Although more detailed studies are required, the conservative approach followed in this research gives confidence that the FC mass is not underestimated with the current method and that the concept proposed is a feasible solution for hydrogen aircraft.

Finally, integrating the detailed sizing method into a multidisciplinary aircraft design tool would provide interesting conclusions at an aircraft level and could be used for aircraft in different segments. Moreover, the method could be extended to allow the study of conical tanks, which can be integrated in the tail-cone of the aircraft. The connection between both tanks and the loads resulting from that interaction should also be included in future studies to increase the detail of this sizing method.

BIBLIOGRAPHY

[1] A. Silverstein and E. W. Hall, *Liquid hydrogen as a jet fuel for high-altitude aircraft*, Tech. Rep. (National Aeronautics and Space Administration Cleveland Oh Lewis Research Center, 1955).

[2] G. D. Brewer, R. E. Morris, R. H. Lange, and J. W. Moore, *Study of the application of hydrogen fuel to long-range subsonic transport aircraft, volume 2*, Tech. Rep. (1975).

[3] G. Brewer, *Advanced supersonic technology concept study: Hydrogen fueled configuration*, Tech. Rep. (1974).

[4] A. Tupolev, *Utilization of liquid hydrogen or liquid natural gas as an aviation fuel,* in *Conference proceedings, project energy, International Academy of Sciences* (1994).

[5] A. G. Rao, F. Yin, and H. G. Werij, *Energy transition in aviation: The role of cryogenic fuels,* Aerospace **7**, 181 (2020).

[6] D. S. Lee, D. W. Fahey, A. Skowron, M. R. Allen, U. Burkhardt, Q. Chen, S. J. Doherty, S. Freeman, P. M. Forster, J. Fuglestvedt, *et al.*, *The contribution of global aviation to anthropogenic climate forcing for 2000 to 2018,* Atmospheric Environment **244**, 117834 (2021).

[7] C. Sky *et al.*, *Hydrogen-powered aviation: A fact-based study of hydrogen technology, economics, and climate impact by 2050,* (2020).

[8] Airbus, *Airbus reveals new zeroemission concept aircraft,* https://www.airbus.com/en/newsroom/press-releases/2020-09-airbus-reveals-new-zero-emission-concept-aircraft (2016).

[9] D. Silberhorn, G. Atanasov, J.-N. Walther, and T. Zill, *Assessment of hydrogen fuel tank integration at aircraft level,* in *Deutscher Luft-und Raumfahrtkongress* (2019).

[10] G. D. Brewer, *Hydrogen aircraft technology* (Routledge, 2017).

[11] D. Verstraete, *The potential of liquid hydrogen for long range aircraft propulsion,* (2009).

[12] C. Winnefeld, T. Kadyk, B. Bensmann, U. Krewer, and R. Hanke-Rauschenbach, *Modelling and designing cryogenic hydrogen tanks for future aircraft applications,* Energies **11**, 105 (2018).

[13] V. K. Mantzaroudis and E. E. Theotokoglou, *Computational analysis of liquid hydrogen storage tanks for aircraft applications,* Materials **16**, 2245 (2023).

[14] A. Gomez and H. Smith, *Liquid hydrogen fuel tanks for commercial aviation: Structural sizing and stress analysis,* Aerospace Science and Technology **95**, 105438 (2019).

[15] J. Huete, D. Nalianda, and P. Pilidis, *Impact of tank gravimetric efficiency on propulsion system integration for a first-generation hydrogen civil airliner,* The Aeronautical Journal **126**, 1324 (2022).

[16] G. Onorato, *Fuel tank integration for hydrogen airliners,* (2021).

[17] A. Elham, *Weight indexing for multidisciplinary design optimization of lifting surfaces,* (2013).

[18] E. J. Adler and J. R. Martins, *Hydrogen-powered aircraft: Fundamental concepts, key technologies, and environmental impacts,* Fuel **32**, 7.

[19] ZeroAvia, *Zeroavia successfully completes initial dornier 228 flight test campaign,* https://zeroavia.com/complete-flight-test/ (2023).

[20] C. van Woensel, *Integration of a liquid hydrogen fuel tank into the concept of the flying-v,* (2021).

[21] S. K. Mital, J. Z. Gyekenyesi, S. M. Arnold, R. M. Sullivan, J. M. Manderscheid, and P. L. Murthy, *Review of current state of the art and key design issues with potential solutions for liquid hydrogen cryogenic storage tank structures for aircraft applications,* (2006).

[22] L. McCullers, *Flops: Flight optimization system,* Proceedings of Recent Experiences in Multidisciplinary Analysis and Optimization, Hampton, Virginia , 24 (1984).

[23] F. M. Troeltsch, M. Engelmann, A. E. Scholz, F. Peter, J. Kaiser, and M. Hornung, *Hydrogen powered long haul aircraft with minimized climate impact,* in *AIAA Aviation 2020 forum* (2020) p. 2660.

[24] H. Klug and R. Faass, *Cryoplane: hydrogen fuelled aircraft — status and challenges,* Air & Space Europe **3**, 252 (2001).

[25] M. Astaburuaga and J. Krijnen, *Conventional aircraft description,* (2001).

[26] S. Wu, J. Li, P. Ding, and Z. Ouyang, *Calculation and analysis of optimal layer density for variable density multilayer insulation based on layer by layer model and lockheed equation,* Cryogenics , 103699 (2023).

[27] J. Huete and P. Pilidis, *Parametric study on tank integration for hydrogen civil aviation propulsion,* International Journal of Hydrogen Energy **46**, 37049 (2021).

[28] T. F. Johnson, E. S. Weiser, B. W. Grimsley, and B. J. Jensen, *Cryopumping in cryogenic insulations for a reusable launch vehicle,* (2003).

[29] D. Verstraete, P. Hendrick, P. Pilidis, and K. Ramsden, *Hydrogen fuel tanks for subsonic transport aircraft,* International journal of hydrogen energy **35**, 11085 (2010).

[30] P. Wang, L. Ji, J. Yuan, Z. An, K. Yan, and J. Zhang, *The influence of inner material with different average thermal conductivity on the performance of whole insulation system for liquid hydrogen on orbit storage,* International Journal of Hydrogen Energy **46**, 10913 (2021).

[31] E. Mendez Ramos, *Enabling Conceptual Design and Analysis of Cryogenic In-Space Vehicles through the Development of an Extensible Boil-Off Model,* Ph.D. thesis, Georgia Institute of Technology (2021).

[32] H. Central, *Hypoint dramatically extends zero-emission hydrogen flight range with new ultralight liquid hydrogen fuel tanks,* https://hydrogen-central.com/hypoint-zero-emission-hydrogen-flight-range-ultralight-liquid-hydrogen-fuel-tanks/ (2022).

[33] NLR, *Liquid hydrogen composite tanks for civil aviation,* https://www.nlr.org/case/case-liquid-hydrogen-composite-tanks-for-civil-aviation/ (2023).

[34] NASA, *Sls fact sheets,* https://www.nasa.gov/humans-in-space/space-launch-system/sls-fact-sheets/ (2022).

[35] E. CS, *25. european aviation safety agency certification specifications and acceptable means of compliance for large aeroplanes cs-25; amendment 12, 13 july 2012,* .

[36] W. P. Fischer, U. Cabulis, V. Yakushin, and A. Laabs, *Internal cryogenic insulation for lh2 tanks of future launchers,* (46th International Conference on Environmental Systems, 2016).

[37] M. Nanninga, *High-fidelity structural sizing method for weight estimation of a flying-v,* (2023).

[38] L. A. Krakers, *Parametric fuselage design: Integration of mechanics and acoustic & thermal insulation,* (2009).

[39] W. Xu, Q. Li, and M. Huang, *Design and analysis of liquid hydrogen storage tank for high-altitude long-endurance remotely-operated aircraft,* International Journal of Hydrogen Energy **40**, 16578 (2015).

[40] W. Johnson, *Thermal analysis of low layer density multilayer insulation test results,* in *AIP Conference Proceedings,* Vol. 1434 (American Institute of Physics, 2012) pp. 1519–1526.

[41] C. Coic, M. Sielemann, D. Andersson, and A. Nguyen, *Fundamentals of aircraft hydrogen tank design with system simulation,* in *10 EUCASS–9 CEAS-The Aerospace Europe Conference 2023* (2023) pp. EUCASS2023–979.

[42] I. Şen, *Aircraft fuselage design study: Parametric modeling, structural analysis, material evaluation and optimization for aircraft fuselage,* (2010).

[43] E. Torenbeek, *Advanced aircraft design: conceptual design, analysis and optimization of subsonic civil airplanes* (John Wiley & Sons, 2013).

[44] F. Irving, *Synthesis of subsonic airplane design. egbert torenbeek. delft university press, delft. 1976. 598 pp. illustrated. dfl. 130.* The Aeronautical Journal **80**, 370 (1976).

[45] T. H. G. Megson, *Aircraft structures for engineering students* (Butterworth-Heinemann, 2016).

[46] T. L. Lomax, *Structural loads analysis for commercial transport aircraft: theory and practice* (American Institute of Aeronautics and Astronautics, 1996).

[47] R. Parello, Y. Gourinat, E. Benard, and S. Defoort, *Structural sizing of a hydrogen tank for a commercial aircraft,* in *Journal of Physics: Conference Series,* Vol. 2716 (IOP Publishing, 2024) p. 012040.

[48] D. Klarholm, *Offset modeling of shell elements: a study in shell element modeling using nastran,* (2016).

[49] K. Al-Rubaie, *A general model for stress-life fatigue prediction,* Materialwissenschaft und Werkstofftechnik: Entwicklung, Fertigung, Prüfung, Eigenschaften und Anwendungen technischer Werkstoffe **39**, 400 (2008).

[50] L. Liao, *A study of inertia relief analysis,* in *52nd AIAA/ASME/ASCE/AHS/ASC Structures, Structural Dynamics and Materials Conference 19th AIAA/ASME/AHS Adaptive Structures Conference 13t* (2011) p. 2002.

[51] J. De Jong, D. Schütz, H. Lowak, and J. Schijve, *A standardized load sequence for flight simulation tests on transport aircraft wing structures,* NLR-TR 73029 U, LBF Bericht FB-106 (1973).

[52] N. Turrel and D. Auriche, *Widespread fatigue damage-a300b: compliance with ageing aircraft regulation,* Airbus Fast Magazine **51**, 17 (2013).

[53] Airbus, *Aircraft Characteristics, Airport and Maintenance Planning* (2020).

A

LOAD DIAGRAMS
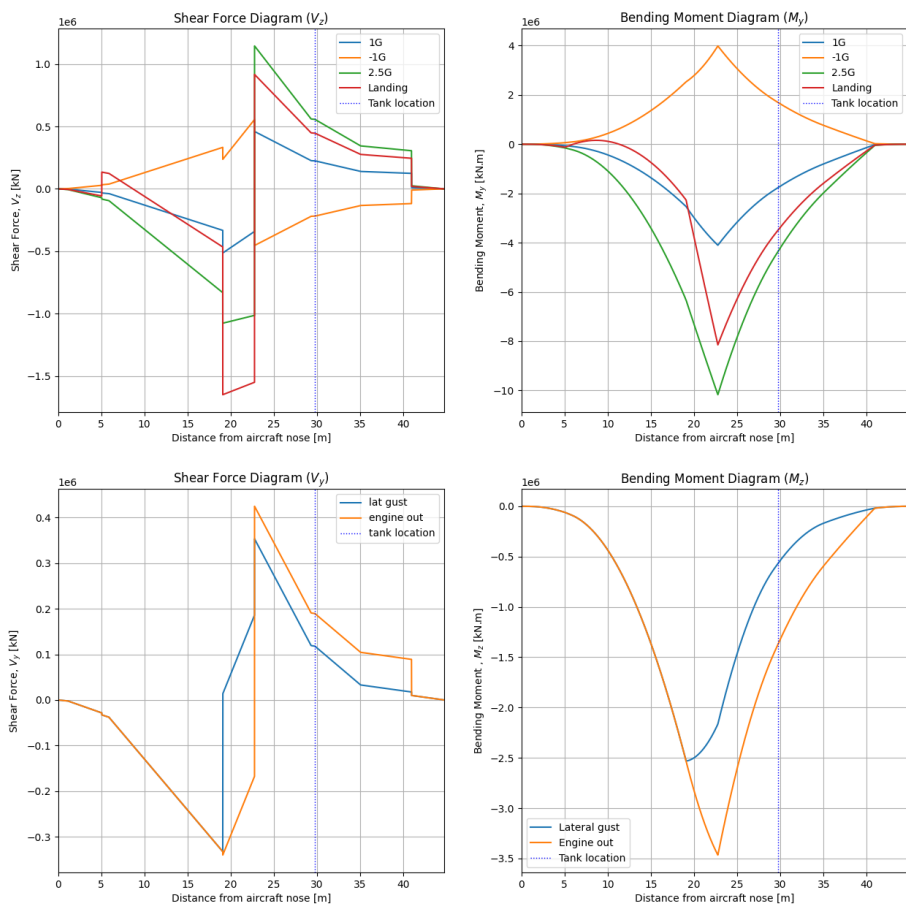
Figure A.1: Shear forces and bending moment distributions for case with single AFT tank
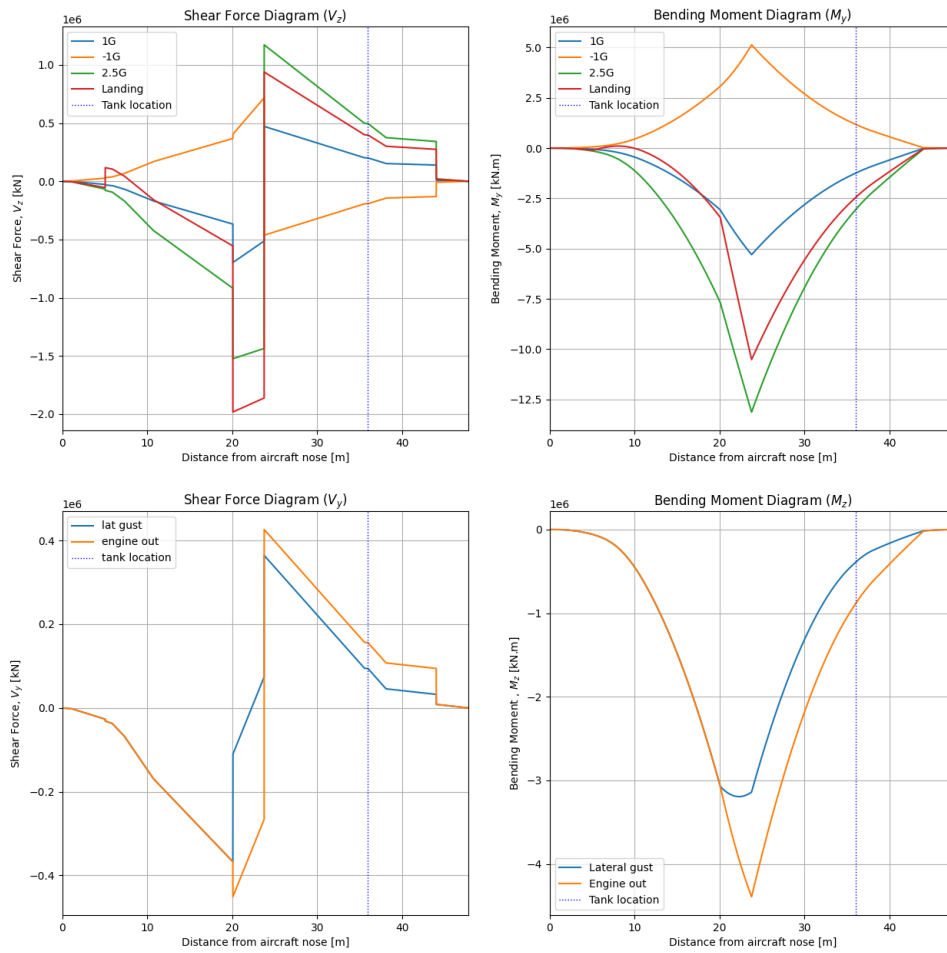
Figure A.2: Shear forces and bending moment distributions for case with FWD and AFT tank

B

DOE RESULTS

Experiment	0	1	2	3	4	5	6	7	8	9
h_{fr}	0.12	0.18	0.13	0.16	0.18	0.18	0.17	0.2	0.16	0.17
n_{str}	68	54	60	28	64	62	22	68	74	42
n_{fr}	21	19	17	14	19	13	24	22	27	22
L_{tank}	9.4	9.9	9.5	9.8	9.9	9.9	9.8	10.1	9.8	9.8
m_{wall_i}	968.7	956.7	966.7	960.6	956.7	956.7	958.6	952.8	960.6	958.6
m_{ins}	151.5	154.7	152.0	153.6	154.7	154.7	154.1	155.9	153.6	154.1
m_f	80.6	87.1	81.7	84.9	87.1	87.1	86.0	89.3	84.9	86.0
m_{wall_o}	1097.4	1333.2	1133.5	1722.5	1211.7	1295.3	2058.4	1326.6	1172.0	1449.6
t_{sk_1}	3.6	4.1	3.9	6.8	3.7	3.7	8.5	3.5	3.4	5.1
t_{sk_2}	3.3	3.8	3.6	6.2	3.5	3.5	7.7	3.2	3.2	4.8
t_{sk_d}	0.5	0.5	0.5	0.5	0.5	0.5	0.5	0.5	0.5	0.5
t_{str_1}	2.2	2.2	1.8	3.3	1.3	2.4	2.6	2.2	1.6	2.0
t_{str_2}	2.2	2.2	1.8	3.4	1.4	1.8	2.5	2.3	1.6	1.8
h_{str_1}	54.6	67.9	72.4	89.5	79.9	85.8	80.3	58.8	53.5	70.0
h_{str_2}	47.3	59.1	62.0	74.1	65.5	81.5	68.8	50.7	46.7	61.5
t_{fr}	1.0	1.0	1.0	1.0	1.0	1.0	1.0	1.0	1.0	1.0
m_{FC}	2576.1	2828.2	2614.5	3249.3	2696.9	2787.3	3611.7	2820.5	2654.7	2954.2
η_{FC}	0.69	0.67	0.69	0.64	0.68	0.67	0.61	0.67	0.68	0.66

Experiment	10	11	12	13	14	15	16	17	18	19
h_{fr}	0.19	0.15	0.18	0.19	0.19	0.18	0.13	0.15	0.14	0.19
n_{str}	34	54	72	22	48	62	20	42	34	48
n_{fr}	23	14	9	16	11	10	11	18	20	10
L_{tank}	10.0	9.7	9.9	10.0	10.0	9.9	9.5	9.7	9.6	10.0
m_{wall_i}	954.7	962.6	956.7	954.7	954.7	956.7	966.7	962.6	964.6	954.7
m_{ins}	155.3	153.1	154.7	155.3	155.3	154.7	152.0	153.1	152.5	155.3
m_f	88.2	83.8	87.1	88.2	88.2	87.1	81.7	83.8	82.8	88.2
m_{wall_o}	1682.1	1198.7	1653.1	2044.7	1524.2	1462.9	2771.0	1387.1	1516.4	1573.7
t_{sk_1}	6.1	4.1	3.2	8.3	4.6	3.6	11.7	5.1	6.0	4.6
t_{sk_2}	5.6	3.8	3.0	7.6	4.2	3.4	7.2	4.7	5.6	4.2
t_{sk_d}	0.5	0.5	0.5	0.5	0.5	0.5	2.8	0.5	0.5	0.5
t_{str_1}	2.2	1.6	3.4	2.7	3.4	3.4	3.6	2.2	2.3	3.4
t_{str_2}	1.7	1.5	3.4	2.3	2.3	2.4	2.4	2.3	2.2	2.7
h_{str_1}	72.9	92.2	113.4	103.6	95.0	99.6	130.0	74.0	74.6	103.4
h_{str_2}	68.1	82.7	98.8	93.1	91.3	94.2	130.0	63.1	63.1	93.7
t_{fr}	1.0	1.0	1.0	1.0	1.0	1.0	3.7	1.0	1.0	1.0
m_{FC}	3204.7	2684.0	3173.7	3596.3	3034.1	2968.2	4383.1	2887.4	3027.6	3087.6
η_{FC}	0.64	0.68	0.64	0.61	0.65	0.66	0.57	0.66	0.65	0.65

Experiment	20	21	22	23	24	25	26	27	28	29
h_{fr}	0.17	0.17	0.19	0.16	0.16	0.17	0.13	0.15	0.13	0.2
n_{str}	76	44	50	38	36	74	78	26	70	58
n_{fr}	15	17	9	23	8	15	26	28	12	21
L_{tank}	9.8	9.8	10.0	9.8	9.8	9.8	9.5	9.7	9.5	10.1
m_{wall_i}	958.6	958.6	954.7	960.6	960.6	958.6	966.7	962.6	966.7	952.8
m_{ins}	154.1	154.1	155.3	153.6	153.6	154.1	152.0	153.1	152.0	155.9
m_f	86.0	86.0	88.2	84.9	84.9	86.0	81.7	83.8	81.7	89.3
m_{wall_o}	1193.3	1413.7	1588.1	1530.4	1663.8	1234.5	1072.8	1844.0	1149.3	1361.8
t_{sk_1}	3.2	4.9	4.4	5.6	5.7	3.3	3.3	7.5	3.4	4.0
t_{sk_2}	3.0	4.5	4.1	5.2	5.0	3.1	3.0	7.1	3.2	3.7
t_{sk_d}	0.5	0.5	0.5	0.5	0.5	0.5	0.5	0.5	0.5	0.5
t_{str_1}	2.3	2.2	3.4	2.3	3.4	2.3	1.5	1.7	2.3	1.7
t_{str_2}	1.6	2.3	2.3	2.5	3.4	2.2	2.0	0.8	1.8	2.3
h_{str_1}	73.7	78.1	113.1	67.5	126.9	74.0	52.6	100.1	84.0	70.3
h_{str_2}	71.1	65.5	108.3	55.0	109.2	64.9	42.2	97.0	78.8	55.4
t_{fr}	1.0	1.0	1.0	1.0	1.0	1.0	1.0	1.0	1.0	1.0
m_{FC}	2677.3	2915.4	3103.2	3041.9	3185.9	2721.9	2549.0	3380.9	2631.6	2858.6
η_{FC}	0.68	0.66	0.65	0.65	0.64	0.68	0.69	0.63	0.69	0.67

Experiment	30	31	32	33	34	35	36	37	38	39
h_{fr}	0.12	0.15	0.12	0.15	0.13	0.14	0.14	0.14	0.14	0.2
n_{str}	46	52	28	24	30	66	80	40	56	32
n_{fr}	25	26	16	20	13	25	24	12	27	18
L_{tank}	9.4	9.7	9.4	9.7	9.5	9.6	9.6	9.6	9.6	10.1
m_{wall_i}	968.7	962.6	968.7	962.6	966.7	964.6	964.6	964.6	964.6	952.8
m_{ins}	151.5	153.1	151.5	153.1	152.0	152.5	152.5	152.5	152.5	155.9
m_f	80.6	83.8	80.6	83.8	81.7	82.8	82.8	82.8	82.8	89.3
m_{wall_o}	1271.1	1311.3	1565.1	1871.9	1593.5	1175.7	1117.7	1409.6	1223.9	1744.9
t_{sk_1}	4.9	4.5	7.0	7.8	6.5	3.7	3.2	5.3	4.1	6.3
t_{sk_2}	4.5	4.1	6.4	7.2	6.0	3.4	3.0	4.8	3.8	5.8
t_{sk_d}	0.5	0.5	0.5	0.5	0.5	0.5	0.9	0.6	0.5	0.5
t_{str_1}	1.8	1.7	1.7	3.4	3.2	2.2	1.6	2.8	1.4	2.5
t_{str_2}	1.7	2.3	1.2	3.4	3.3	2.3	1.5	1.8	2.2	2.3
h_{str_1}	60.7	60.6	105.7	74.3	90.6	49.9	55.4	91.9	60.7	84.9
h_{str_2}	54.4	46.4	103.0	59.2	76.4	43.3	47.8	90.9	43.4	72.7
t_{fr}	1.0	1.0	1.0	1.0	1.0	1.0	1.0	1.0	1.0	1.0
m_{FC}	2763.7	2805.7	3081.2	3411.0	3111.3	2659.6	2596.9	2912.3	2711.7	3272.2
η_{FC}	0.67	0.67	0.65	0.63	0.65	0.68	0.69	0.66	0.68	0.64